Master of Science in Applied Geophysics

Application of Sentinel-1 data to quantify Arctic Coastal Retreat

Master Thesis
Henry Holsten

Matriculation number - 19-944-149
Date of submission - 13.08.2021

Supervisors

Philipp Bernhard

Institute of Environmental Engineering, ETH Zurich

Prof. Dr. Irena Hajnsek,

Institute of Environmental Engineering, ETH Zurich

Abstract

In the arctic region many coastal areas exhibit rapid erosion, with coastal retreat or erosion rates of 10 meters per year (m/yr.) or higher in places. This poses a threat primarily to all manner of infrastructure built directly on and near the coastline. With climate change the coastal erosion is expected to increase. This effect is expected to be especially severe in the continuous permafrost region, as the coastal erosion is linked with the increase in thermoerosion of the permafrost. A remote sensing method with high coverage and sufficient temporal observation frequency at lower cost than from aerial photography would be practical to mitigate the problem. This would enable assessing and predicting (potential) damage to existing infrastructure and planning of its future locations. A thresholding method based on TerraSAR-X x-band synthetic aperture radar observations is applied to lower resolution Sentinel-1 c-band synthetic aperture radar observations monitor the coastal erosion rates. This study aims to determine the feasibility of using this method with Sentinel-1 data. For this purpose, the method is applied to Senteinel-1 Backscatter scenes and the Coherence between scenes within each year from 2016 to 2020 at three sample sites on Herschel Island (Beaufort Sea, northern Canada). The method was successfully applied to the Sentinel-1 Backscatter data, yielding reliable and accurate results for one of the sample sites, with the highest estimated erosion rate of the three sites. The same technique was applied to the Coherence data. The obtained results were less reliable compared to the results from the Backscatter data, showing too high variance. The results indicate that the application is generally limited to the summer season and to coastlines oriented towards or parallel to the looking direction of the SAR sensor. The results are compared to previous studies of coastal erosion rates on Hershel Island or the nearby northern Yukon coastline region.

Acknowledgements

Thank you to my supervisors, Bernhard Philipp, and Prof. Dr. Irena Hajnsek, for supporting my thesis project. I would like to thank my wife Qinghua Wang (now Holsten), Feliks Kiszkurno as well as the other Applied Geophysics students. I would like to thank my sister Anna Holsten for checking the text quality and my parents Christian and Ruth Holsten for their personal support. Lastly, I would like to thank especially the members of the examination board of the Applied Geophysics programme for granting me an extension of the project on short notice.

Contents

1 Summary

Chapter 2 begins with an introduction to the problem addressed by the study. After a brief introduction to some previous studies and methods, the new approach using Sentinel-1 SAR data is motivated, mainly outlining the advantages in terms of reliability and availability.

Chapter 3 outlines the study area to which the new method will be applied. Firstly, a description of the geography of Herschel Island and the time frame for the observations is given, which begin in 2016. The possibility of adding future Sentinel-1 SAR observations each year is considered as is comparison and of other SAR satellites wither higher spatial resolution. The limits of data usage due to availability of observations in sufficient resolution. Following a brief description of the geology and characterizing the permafrost formations, some resulting coastal erosion features are introduced. The next subsection goes on to explain why this makes the Island particularly suited as a monitoring target using SAR. Lastly the positioning of three study sites for which monitoring results were generated across the Island are displayed on an overview map.

Chapter 4 shows in more detail the method used for two different types of information, namely the Backscatter and Coherence are used to monitor coastal retreat. This is performed by estimating coastline positions between 2016 and 2020. The first and second section explains the processing to generate filtered and appropriately projected SAR Backscatter scenes from the raw single-look complex (SLC) data using the sentinel application platform (SNAP). In the third part, the thresholding approach from Stettner et al. (2017) is illustrated, on which the coastal erosion rate evaluation is based. The implementation and adaptation of this thresholding approach with ArcGIS used for this project is further described then in the fourth section. The fifth and sixth section outline the thresholding applied to Coherence data and the generation of stacked Coherence scenes from the raw data for each year. The seventh and last section details the evaluation with DSAS and use of the results for prediction.

Chapter 5 displays the results of the distance measurements used for coastal retreat monitoring, for both the generated Backscatter and Coherence data. The results from observations made on ascending and descending orbits from the summer (June-September) season are compared for the three study sites. The predicted coastline positions for 2025 are shown as well as comments on the data quality and reliability.

Chapter 6 discusses the results and explores the main factors required to generate accurate coastal retreat rates. Firstly, the effect of the winter and summer season related to the presence of sea-ice on the coastline is considered. Furthermore, the variable efficacy of the thresholding approach is analysed. Next the effect of the second main factor, the sensor orientation compared to the coastline, is assessed by comparing results from the two different orbital path directions. Finally, the effect of the data quality and (weather-related) noise in the image is discussed.

Chapter 7 concludes the discussion, highlighting the main results in terms of the main factors for the accuracy and feasibility examined in C**hapter 6**.

Chapter 8 gives an outlook towards future use of this method using Sentinel-1 SAR and possibly data with higher spatial resolution.

2 Introduction

2.1 The coastal erosion problem under climate change motivating the monitoring of coastal retreat

The arctic permafrost region is one of the fastest-warming regions in the world. A mean temperature increase by 2.3°C was observed between 1948 and 2016 in northern Canada, Bush & Flato (2019). In particular the area around Herschel Island is predicted to see one of the largest temperature increases in the Canadian Arctic, Lantuit and Pollard (2008). The subsequent increase of seawater temperature, which relates to reduced sea ice cover in the arctic ocean, makes this region more vulnerable to wave erosion. This stems from the increased wave action, which is mainly caused by the reduction in sea-ice extent (Nielsen et al. 2020). This is due to the wave-based erosion being present only during the open-water season as mentioned, Lantuit and Pollard (2008). Additionally, shallow permafrost in the sediment immediately at the coast will thaw, steepening the nearshore profile and causing waves to break more directly on the coast, Dallimore et al. (1996). According to Cunliffe et al. (2019), specifically coastal erosion of permafrost regions presents one of the most noticeable and problematic features of the changes occurring. These changes are expected to impact the northern shores in the arctic circle especially.

Figure 1 Varandei oil terminal at risk by wave-cut cliff on the coast of the Pechora Sea Ogorodov (2005).

The study area is a good example for this. It is home to several historic structures from European settlement and is the home of the Inuvialuit who have been inhabiting the island for thousands of years Yukon Government (2021). The coastline adjoins the logistic base for Herschel Island Territorial Park operations and a gravel spit where culturally significant sites are located. The importance of monitoring (and predicting) coastline erosion will continue to increase, with community expansion and demand for arctic resources leading to an increase in the amount of permanent infrastructure in the arctic region, particularly in coastal areas. There have already been disruptions of infrastructure resulting from coastal erosion, making coastlines a management priority after 1950 Solomon (2002), Johnson et al. (2003). This is especially relevant as human factors and structures can double coastal rates, putting these structures at higher risk of collapse by erosion of ground beneath, see Figure 1. This was observed for example at the coastline on the Pechora Sea coast, northern Russia, SE of the Barents Sea. This linked to the intensification of eolian (relevant for coastal regions with loose sediments such as dunes), slope and thermoerosion processes. This is a result of factors such as removal and destruction of ground cover from vehicle use Ogorodov, (2005). The increasing damage makes monitoring the retreat rates a major task in mitigating further damages and plan structural (re)location. A monitoring method for coastal retreat using satellite images could provide reliable, long-term, and large-scale monitoring of coastal erosion. This could provide large advantages over ground-based or airborne imaging in terms of cost and time investment, particularly if most steps could be performed (semi-)automatically.

2.2 Previous large-scale approaches

There have been many different approaches to monitoring landscape and coastline changes in the arctic region on different timescales and vastly different geographic scopes. SAR data has seen multiple applications towards assessing coastal retreat and other forms of erosion in the arctic using different products from which different types of information can be gleaned. Here various previous, large-scale approaches using mainly (In)SAR or optical satellite imagery, or ground-based monitoring are considered.

Short et al. (2011) compared TerraSAR-X, RADARSAT-2 and ALOS-PALSAR interferometry on Herschel Island to monitor ground movement. Interferometric SAR (InSAR) data was used to monitor ground displacement over and within each summer season as good Coherence was maintained for all three sensors during the summer. Overall, interferometry could be performed with data from acuisitions several years apart except for data from TerraSAR-X, which is of more use for permafrost monitoring than short-term change detection. They found ground displacement of 20 to 30 cm/yr. mainly on the north-eastern coastal slopes, the slope stability also being affected by coastal erosion. Monitoring rapid topographic change, such as thaw slumping or coastal erosion was mentioned as not feasible; it was suggested that a different method such as Coherence loss mapping would be more applicable here.

Bartsch et al. (2020) explored the feasibility of applying SAR to monitor coastal erosion in the entire arctic using multiple satellite platforms and radar wavelengths: X-, C-, L-band from TerraSAR-X, Sentinel-1, ALOS PALSAR 1/2. SAR has the advantage as the imaging is largely unaffected by cloud cover compared to optical wavelength satellite imagery. The results between SAR platforms and optical Landsat imagery are compared in the study. Disadvantages of SAR imaging result from ambiguities in ground Backscatter properties and viewing geometry considerations as well as differences in spatial and temporal coverage between platforms. Results from all three wavelengths have been evaluated at steep coastal cliffs on Herschel Island. These are compared with annual erosion rates of 0.5 to 1.2 m/yr. from Lantuit et al. (2012). Bartsch et al. (2020) also mention the earlier ERS-1/2 (European remote sensing satellites 1 and 2, 1991–2011) and JERS-1 (Japanese Earth Resources Satellite 1) satellite missions, but these results are not considered as they have comparatively coarse spatial resolution of 18m at best. Here the linear relationship of Backscatter intensity (σ_0) with the local incidence angle was explored. With the local incidence angle relationship is calculated based on slope and line of sight (LOS) gradient. Data from both ascending and descending orbit passes was used, enabling comparison of results based on cliff-top classification with land-water classification at Herschel Island. As in this study, a modified thresholding method is applied, based on the method from Stettner et al. (2017). The separability between land and water σ_0 values is better for data acquired during the summer than during winter as is also found in this study. The results are listed in Table 3.

Orthorectified aerial photogrammetry and an IKONOS satellite imagery was used by Lantuit and Pollard (2008) to quantify coastal retreat on Herschel Island between 1952 and 1970 as well as 1970 and 1990. The images were processed to obtain a ±2m horizontal accuracy for estimating retreat rates. They also explored a possible link between retrogressive thaw slumps and increased erosion rate at the coast below these. Contrary to expectations based on previous study by Lantuit and Pollard (2003) showing an increasing coastal erosion rate, in Lantuit and Pollard (2008) a decreasing coastal erosion rate is observed, see Table 3. Here over 50m total erosion for exposed shores is calculated for both time intervals between images. The different rate estimates may be due to a decreased number of storm events since 1980, from Solomon (2005) and lower proportion of storms from the North-West. The disagreement in results from McDonald & Lewis (1973) and Lantuit and Pollard (2003) may have resulted from different measurement points used and use of unrectified imagery. This may also be due to aerial photography being scarce for the Herschel Island region since 1980, leaving high-resolution optical satellite imagery (i.e., from IKONOS, Quickbird) to derive erosion rate estimates, see Lantuit and Pollard (2008).

2.3 Previous local-scale approaches

Here, monitoring approaches using drone imagery or ground-based monitoring are considered.

Close comparison of the results from this study can particularly be made to the results from a drone survey Cunliffe et al. (2019), see Chapter 6. In their study, the intra-annual and short-term erosion was determined to be up to 1.1 m/d. over a stretch of 500m at Site 1 (see Chapter 3 for location). The long-term increase in observed coastal erosion rates compared in their study is mainly attributed to rising air temperature and increasing length of open-water season.

Stettner et al. (2017) measured the erosion rate of the cliff-top on the bank of the Lena River Delta in 2015 using wooden stakes placed every 50cm to validate the results from the TerraSAR-X time series.

2.4 Why is Sentinel-1 C-band SAR particularly suitable for monitoring ACR?

Sentinel-1 SAR data has multiple advantages in terms of coverage and observation frequency over other sources of data for monitoring ACR. Long-term records of erosion are described as scarce by Lantuit and Pollard (2008), especially in the Canadian Arctic and predominately cover only specific regions within it. Compared to this, Sentinel-1 covers the whole arctic with a revisiting time of 12 days. Sentinel-1 SAR data may not achieve the same resolution with ≈5m spatially compared with for example ≈2m from optical data – depending on sensor used, yet it has two advantages over the optical satellite imagery. The first is the near independence from weather conditions; the relevance of this depends on the e.g., the cloud cover and the quality of SAR images dependent on the time of year. The second advantage in practical terms is the open availability of the data. The Sentinel-1 raw data can be downloaded free of charge, for example from the NASA Earth data open access platform or the Copernicus open access hub. Optical imagery in high resolution is not expected to be free or have the same coverage and continuous recording. Sentinel-1 data is available for observatio0ns beginning in 2014, with continuous records from ≈2016.

The Sentinel-1 mission is part of the European Space Agency’s (ESA) Copernicus initiative. It consists of two satellites on the same sun-synchronous orbit separated by 180°, such that they are on opposite sides of the Earth. Each satellite (S1-A and S1-B) has a repeat-pass time of 12 d, which depending on Imaging mode has a combined worldwide coverage every 6 days. The data used for this study is captured in IW imaging mode, see Figure 2.

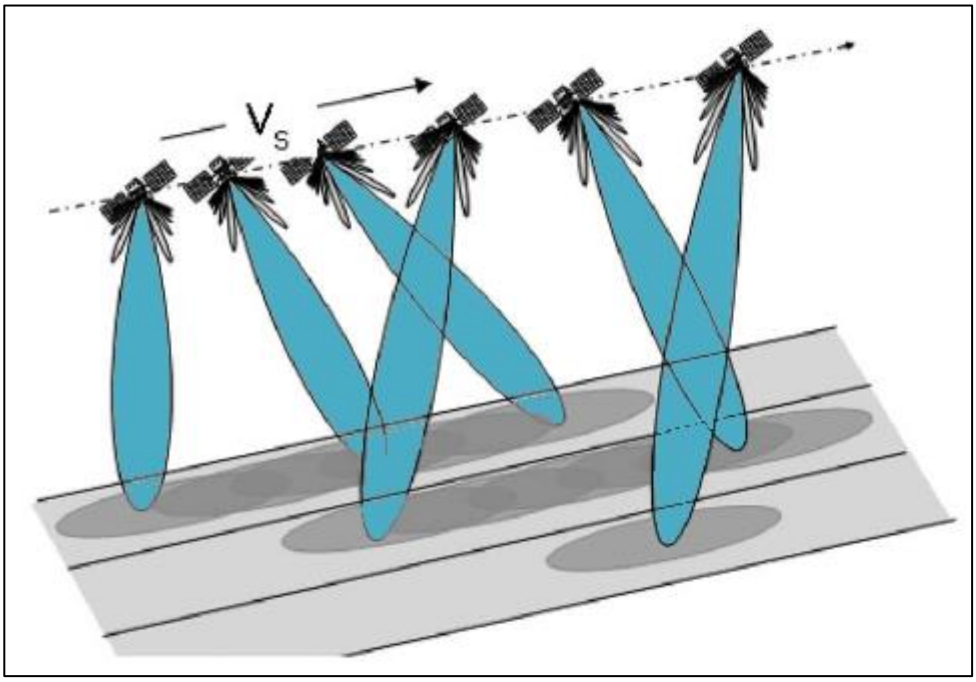

Figure 2 the antenna footprint pattern for the Interferometric-Wide Swath (IW) imaging mode of Sentinel-1 c-band SAR. It is the main acquisition mode for this mission, with data acquired near continuously since 2016, with the first available scenes from 2014. All datasets for this study have been acquired using this imaging mode. Source: The European Space Agency Sentinel-1 User Guide, De Zan & Guarnieri (2006), see bibliography for link.

2.5 Objective: Monitoring Coastline erosion

The objective of this project can be broadly summarized as to demonstrate the viability of using readily available, open-source C-Band (In)SAR data to derive shoreline positions with sufficient accuracy. A key question here is: Will the thresholding method based on Stettner et al. (2017) be viable to produce accurate results considering the low resolution? The aim is that these approaches may be applied to other areas with the parameters adjusted to the given data. In practice the focus lies on building simple workflows to generate these results in a manner which does not require high levels of computing resources and large time investments. Ideally it should be feasible to generate results on the scale of a small region without requiring cluster-level computing resources within reasonable time. The estimated planimetric erosion rate and prediction of short to mid-term. This could be up to an estimated 5 years for the given time interval, but possibly further with more data in the future, which is naturally also subject to data quality and result accuracy. Coastline positions can serve as the first-order basis for various decisions, for example the planning for locations of permanent facilities close to the coast around the arctic permafrost region. The results also represent a way to assess the further impact of global warming on the development of coastlines and land loss due to global warming, particularly when compared to historic erosion rates.

3 The Herschel Island study area and geographic & temporal scope

3.1 General characteristics of the study area

The geographic scope of this project is limited to Herschel Island as the directly studied area of interest (AOI). The Island is located 5 km off the northern coast of Yukon, Canada, with an estimated surface area of ≈116km² and ≈50km coastline. It is position at 69.5833°N, 139.0226°W in the southern Beaufort Sea, Mackay, (1959). It is 15km by 8km in extent with a maximum elevation of 183m above MASL, Mackay (1959). The time scope of this study covers 2014 to 2021; New data can be used as it is acquired in the future. This will also increase the overall reliability and accuracy of the estimates of coastline positions.

The geology of the island is composed largely of marine terrigenous sediments originating from the Herschel Basin (Beaufort Sea) and therefore consists of fine-grained marine terrigenous sediments such as diamicton with some coarser material, from Lantuit and Pollard (2008). The island was formed by ice-pushing of these sediments by the Laurentide ice sheet during the Wisconsin Glaciation, see Mackay (1959).

3.2 Characteristics of Permafrost and suitability as a target for coastal erosion monitoring

Herschel island is particularly suited as a study site due to its geology and permafrost setting, which is noted for its vulnerability towards rising temperatures through permafrost degradation as noted by e.g., Short et al. (2011). The island lies in the continuous permafrost zone is considered to be covered by several hundred meters deep permafrost in light of the high thickness of the permafrost in this coastal region. This is up to 600m according to Smith and Burgess (2000). The active layer on the surface is up to 0.6m thick on most of the area of fine-grained sediments and maximally 1.1m thick (Smith et al., 1989). The active-layer thickness is expected to increase as the permafrost warms, Lantuit and Pollard (2008). The surface contains many permafrost structures such as ice wedges, lenses, buried and massive ice structures; with some of these being glaciogenic in origin. This matches up well with the high ground-ice content of 60-70% in the uppermost 12m of permafrost, with intrasedimental ice being the most common massive ground ice. This is based on sediment and ice samples from Pollard (1990). Numerous thaw structures such as large retrogressive thaw slumps and polycyclic thaw slumps have already been observed by Pollard (1990), with high density on the southern side of Herschel Island.

3.3 Coastal and other erosion features.

Figure 3 Left: aerial photo of a retrogressive thaw slump with Headwall and Scar zone indicated, from Bernhard et al. (2020). Right: Cliff-base erosion as an effect of wave- and thermoerosion undercutting the top layers, leading to block failure visible as fallen blocks on the right side of the image, from Hoque and Pollard (2016).

Apart from direct retreat of the coastline landwards, there is two main features which are closely associated with coastal erosion. The first is retrogressive thaw slumps (RTS), see left image in Figure 3, which form above the coast with the South-East facing shorelines showing the highest density of these, Lantuit and Pollard (2008). The second is block failure caused mainly by permafrost thawing and undercutting of coastal cliff by wave action, see right side of Figure 3. A RTS forms by melting of permafrost followed by the subsequently resulting ground subsidence, which exposes the frozen ground from the side which then represents a headwall as it is relatively higher than the thawed mud. The exposed headwall thaws much faster and retreats up-slope. The numerous thaw slumps concentrated on the southern side of Herschel Island, Pollard (1990), may be related to the higher erosion rates observed on South and south-eastern shores. The slumps lower the cliff profile. With the resulting mudflow and sorting of sediments leaving behind ground ice below the slump floor and temporarily caused progradation of the coastline due to the sediments flowing out to the sea. The remaining structure has significantly increased vulnerability to wave action and thermoerosion. The highest erosion rate result is therefore expected to be observed on the South facing parts of the three study sites for which erosion rates are calculated.

This shows that the island is actively being eroded, its topmost permafrost layer by degradation and thaw and at its shorelines furthermore also through wave action. This erosion is expected to accelerate along with the increased rate of climate change.

3.4 Suitability of SAR Backscatter for monitoring coastal retreat on Herschel Island

The islands surface is covered by vegetation and composed of a mixture of ground ice and small-grained sediments. The high width compared to height and gentle topography prevents spatial ambiguity such as layover and foreshortening almost entirely in the SAR scenes Short et al. (2011). Directly at the coastline and at somewhat rougher topography some effects are expected, however. In addition to its low topography, the island is covered in low tundra vegetation (e.g., Short et al. (2011)). This results in mostly homogeneous radar Backscatter properties across the land surface, making it a good target for classifying by threshold. Based on this, the study area is a good choice for achieving the objective of this study. The land area is generally expected to be well-delineated in the SAR scenes due to the Backscatter difference between water and land surface at least seasonally. The SAR scenes should then reliably display the boundaries between land and water and not be affected by ambiguity resulting from the viewing geometry for the SAR ranging technique. The simple workflows can then be applied without high levels of adjustment to data from multiple years, yielding a time series of shoreline positions at given sites.

3.5 Study sites on the Coastline of Herschel Island and temporal scope

From this study area, three sample sites are selected, see map on Figure 4 for relative location:

1. Cunliffe: A 600m stretch of coastline termed this way as it contains the study site from Cunliffe et al. (2019) mapped with drone imagery. This site is selected as the results of this study can be more directly compared to the results of the drone imagery than to results of other studies.
2. Westside site: A 1km stretch of near completely straight coastline facing close to exactly westwards at Orca Cove.
3. Eastside site: A 1km stretch of curved coastline on the south-eastern end of Herschel Island covering the coastline at the North side of Collinson Head. Study sites 2 and 3 are chosen to assess the effect of sensor orientation relative to the coastline that is being mapped.

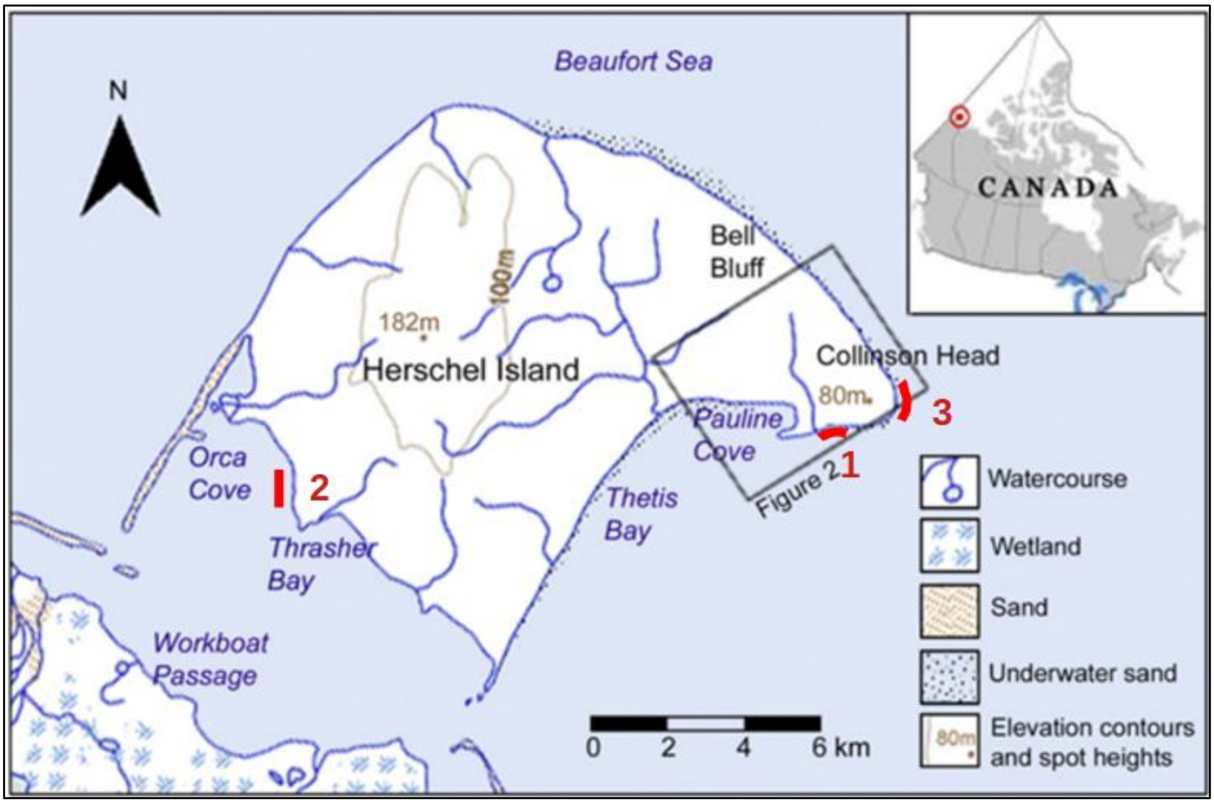

Figure 4 Overview map of Herschel Island with basic geographic features from Short et al. 2011 with its position within Canada shown in the inset (top right), modified from National Topographic Mapsheet 117D. The relative baseline positions for each sample site of this study are marked with short red lines and are numbered

4 Methods

4.1 Using Backscatter thresholding to monitor coastline positions

To produce estimates of the coastline position and erosion rates, four main steps are required:

1. Processing the raw SAR data to produce a two-dimensional image of Herschel Island from the σ_0 or Coherence values.
2. Applying the thresholding method to the σ_0 - and Coherence images with the modelbuilder toolbox in ArcGIS.
3. Using the DSAS extension to measure the position at each site for each year represented by the line objects showing the threshold boundaries in the images
4. Using Excel to smooth, visualize and check the quality of the results, such that they can be used for the evaluation of coastal erosion rates and the uncertainty of the results.

4.2 Pre-processing of Synthetic Aperture Radar Backscatter data within the Sentinel Application Platform (SNAP)

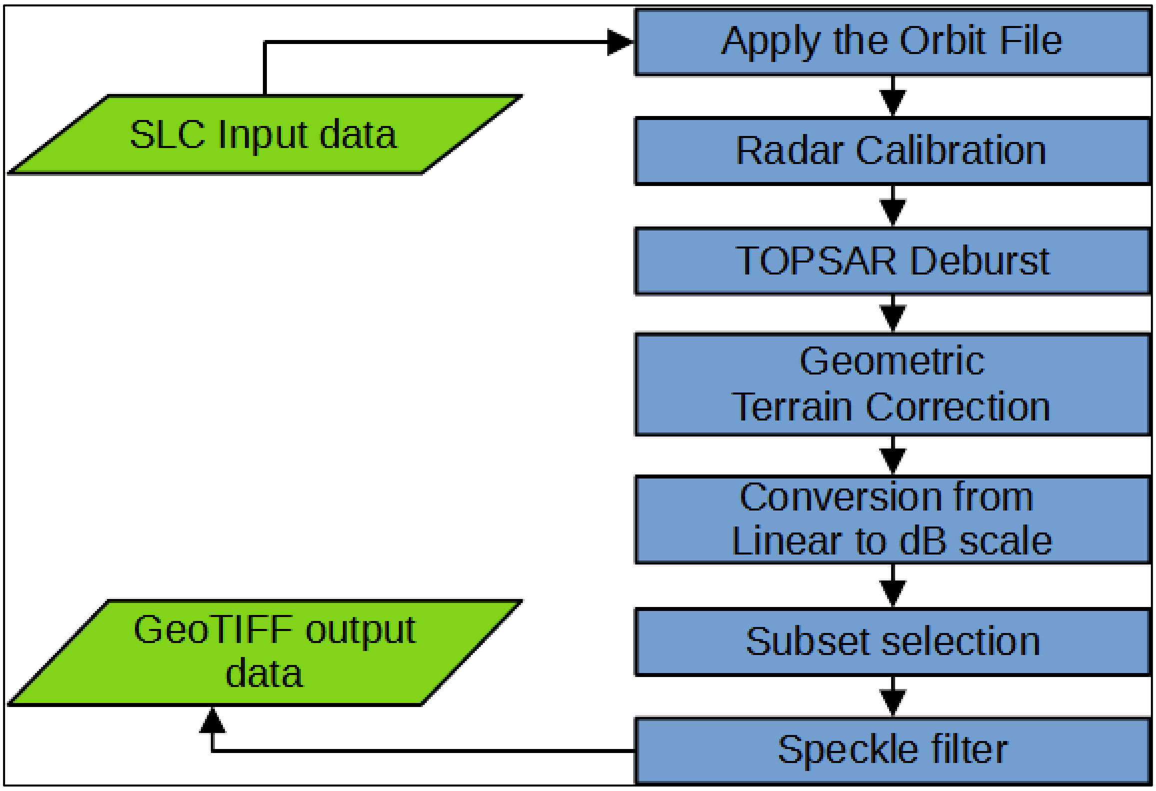

Figure 5 Sentinel Applications Platform processing chain. The SAR data is written to a GeoTIFF after being mapped to the desired projection and filtered.

The processing begins with the selection of data fitting the geographic scope and the selected time of year as well as some parameters regarding the acquisition of data. The data used here is acquired on an ascending orbit in IW mode. The polarizations used for this project are vertical-vertical (VV) and vertical-horizontal (VH). The data is obtained from the Alaska Satellite Facility, the selection is made by setting the filters to the desired area and time interval as well as acquisition parameters. The data is downloaded and input into the flowchart with the read function as unprocessed SAR data. The files come in ZIP format and contain the individual subswaths of the Single-look Complex (SLC) data acquired in IW burst mode.

To accurately map the data to the correct locations, the orbital information must be applied to the data based on time of acquisition. The first processing step is to map the orbital path information to the data such that the radar signal scattered back to the receiver from each pulse is assigned to the correct geographic location based on timing and sensor position. This is performed by applying the orbit file to the complex-valued data.

The Backscatter intensity is calibrated from the raw intensity output, which is altered by the SAR processor which is necessary to achieve both high azimuth and high range resolution relative to the actual km-scale signal footprint (shown schematically in Figure 2). The rescaling attempts to remove the patterns caused by the SAR processor while considering the geometric scaling of the signal with range, for which an additional gain is applied.

The SAR scenes come in three bursts, with multiple datasets on each of 9 subswaths in a burst are acquired for the same azimuthal along the orbit.

Debursting is the process of removing the antenna pattern from the SAR scene. This is accomplished with the Sentinel-1 TOPS Deburst tool in SNAP. This assigns the subswaths to the correct relative position within the SAR scene by shifting and aligning the subswaths relative to each other. The subswaths then form a contiguous image, with the overlapping part interpolated or averaged.

The radar data consists of intensity and timing information which represents the slant-range or direct range between sensor and objects which scatter the radar pulses back to the sensor. This information must be projected to the correct ground range. This requires information about the correct topography to disperse ambiguous arrival times to correct possible locations. This will not be 100% reliable, as it is a (albeit not heavily, depending on geometry) underdetermined inverse problem. The topographic information is supplied by an Interferogram-generated DEM from the ALOS-PALSAR mission, see Tadono et al. (2014) for details. This has a resolution of 20m in E-W direction and 30m in N-S direction, which is accurate enough for the terrain correction. The result should be a reliable and accurate conversion, especially considering the flat topography, such that height errors and range ambiguity are low. In this step data is converted from the slant-range viewing geometry that it was acquired in to ground range or cartesian coordinates and then projected to a specific coordinate system. For this project, the selected coordinate system was EPSG: 3995 – WGS 84 / Arctic Polar Stereographic. This coordinate system was chosen with respect to the far-North study site as it is useful to display the data in both SNAP and ArcGIS. As Herschel Island is above 65° Latitude North this also avoids the large geometric distortion observed with more common coordinate projections such as the WGS84 projection in decimal degrees. At this step only the real-valued Backscatter intensity, termed σ_0 is saved as an output band.

The σ_0 values vary over 5 orders of magnitude over a linear scale; they are converted to the logarithmic decibel scale for better overview and faster visual evaluation and control of processing results. This is convenient for the subsequent processing within ArcGIS as well. The logarithmic scale gives a much better sense of the intensity distributions in the data (see Figure 30), showing logarithmic-gaussian distribution types. It reduces the value range from 4-5 orders of magnitude to 1-2.

A speckle filtering step is performed to ideally remove, but more practically attenuate the high level of noise present in real unfiltered SAR data. The random speckle effect or noise in the observed SAR data results from the surface roughness and other effects inherent in the two-way travel time of the backscattered microwave pulse and is always present in real SAR data. As a result of this, the arrival time changes unpredictably, and the corresponding change of phase and Backscatter amplitude shows large variation relative to its maximum as it is scaled with a sinusoid based on the phase. The surface roughness of even the low tundral vegetation and minorly uneven ground is significant compared to the c-band wavelength range of 3.75-7.5cm, especially on the coastline area, which is expected to be rougher due to the erosion. It is then vital to minimise the speckle effect to accurately delineate the coastlines of Herschel Island. An important consideration here is to preserve the image characteristics important for the classification of the image to determine the location of the coastline. Multiple filters have been tested for their image-preserving and filter performance characteristics. Morphological speckle filters such as Simple Alternative Filter or Multiple Structuring Element Filter can be used to largely remove the noise based on imaging target geometry, Kupidura (2005). Based on the results from filtering the Backscatter data used here with the available options within SNAP, see Figure 44, a Frost filter with a small 3˟3-pixel window size and a damping factor of 2 is chosen. This filter is based on Frost et al. (1982) using a minimum mean square error approach based on simple statistics of the data within the filter window. The Frost filter is chosen for this study based on the excellent feature-preserving qualities of this statistics-based filter despite its lower speckle suppression capability, Kupidura (2005).

From the large, ~2GB sized VV or VH Backscatter bands of the SAR scenes a smaller subset is selected. This selection is based on geographic area containing the area of interest. This AOI covers Herschel Island with all parts of its coast and spits and some of the surrounding sea and a small portion of the northern Yukon Coastline. This selection is geometrically based on a simple rectangle polygon as this is a convenient and efficient way to select a specific area within SNAP. Reducing the image to the AOI gives a better overview over the important features for this study and reduces processing and loading time for subsequent use in ArcGIS.

The pre-processed Backscatter is included for VV and VH polarisations as well as the calculated local incidence angle from the Terrain Correction step. This Backscatter raster is now the input for the thresholding method applied with ArcGIS.

4.3 A description of the process for automatic line extraction method from Stettner et al. (2017)

The method to estimate erosion between acquisition is based on Stettner et al. (2017). It is used in this study to perform automatic extraction of the cliff-top lines within a specific stretch of coastline. The first step here is to evaluate the Backscatter intensity visually and statistically on the active cliff area and other surfaces to determine the threshold to classify the area into active cliff area and other surfaces. The threshold of -10.5 dB chosen based on the difference between the mean Backscatter intensity over the tundra above the cliff and of the active cliff area did not accurately classify the areas. The threshold value was then chosen visually, by evaluating which threshold value resulted in the most accurate and correctly classified the active-cliff area pixels and other surfaces by Stettner et al. (2017). The active cliff area is assumed to be the area of highest Backscatter intensity due to the corner or double-bounce radar reflection when the cliff-face is facing towards the sensor. The separation of Backscatter intensity between active cliff area and non-active cliff area and thereby the differentiation based on simple thresholding is enhanced by foreshortening when the cliff-face is aligned towards the sensor. The foreshortening occurs due to the steep angle of the active cliff area compared to the water and top of land surface, resulting in a close to perpendicular incidence angle on the active cliff area. The computational implementation of the following steps is in the ModelBuilder toolbox from ArcGIS^{TM} (ESRI© 10.3.1).

Once the threshold is determined, it is used to classify the pixels in the Backscatter image by assigning the values to 0 and 1 to them, representing the active cliff area with 1 and other areas with 0 as shown in Figure 6, upper row middle column. As this classification is based only on intensity, many pixels that are classified wrongly can be observed both within the active cliff area and the tundra. Conversely, the sea area has the lowest Backscatter intensity, such that it is close to perfectly classified. The individual pixels and small clusters of pixels are filtered out using opening and closing morphological filters. These are applied with a step size of 1 pixel increase and decrease of thickness around the pixels in two steps, see Figure 6 upper and lower right image. In the first of these steps a closing filter is used, which expands the areas of pixels with the value 1 by a given extent in pixels and then shrinks or erodes the features by the same extent, which smooths features and removes the small, misclassified areas within the active-cliff area. In the second filter step an opening filter is applied, which performs the operations of the closing filter but first reduces the size of features, removing the small clusters of pixels with high Backscatter from the tundra area in the image.

Having obtained and accurately classified the active cliff area outline, the image is converted to a polygon so that it can readily be used for distance calculations; the conversion is carried out by construction of lines on all boundaries between the square pixels with different values, see Figure 6 lower row middle column. The polygons are simplified using the approach from Douglas and Peucker (1973) to avoid introducing small step-functions. These result from the conversion along the as it is performed along the boundaries of the by default square pixels in ArcGIS.

From the now cleanly outlined active-cliff area, the line representing the clifftop is selected from each image from the series of acquisition times to estimate the planimetric (area) erosion rate within the AOI. Based on this the erosion rate is predicted using the uncertainty within the extracted line positions with the ArcGIS extension DSAS (v. 4.1).

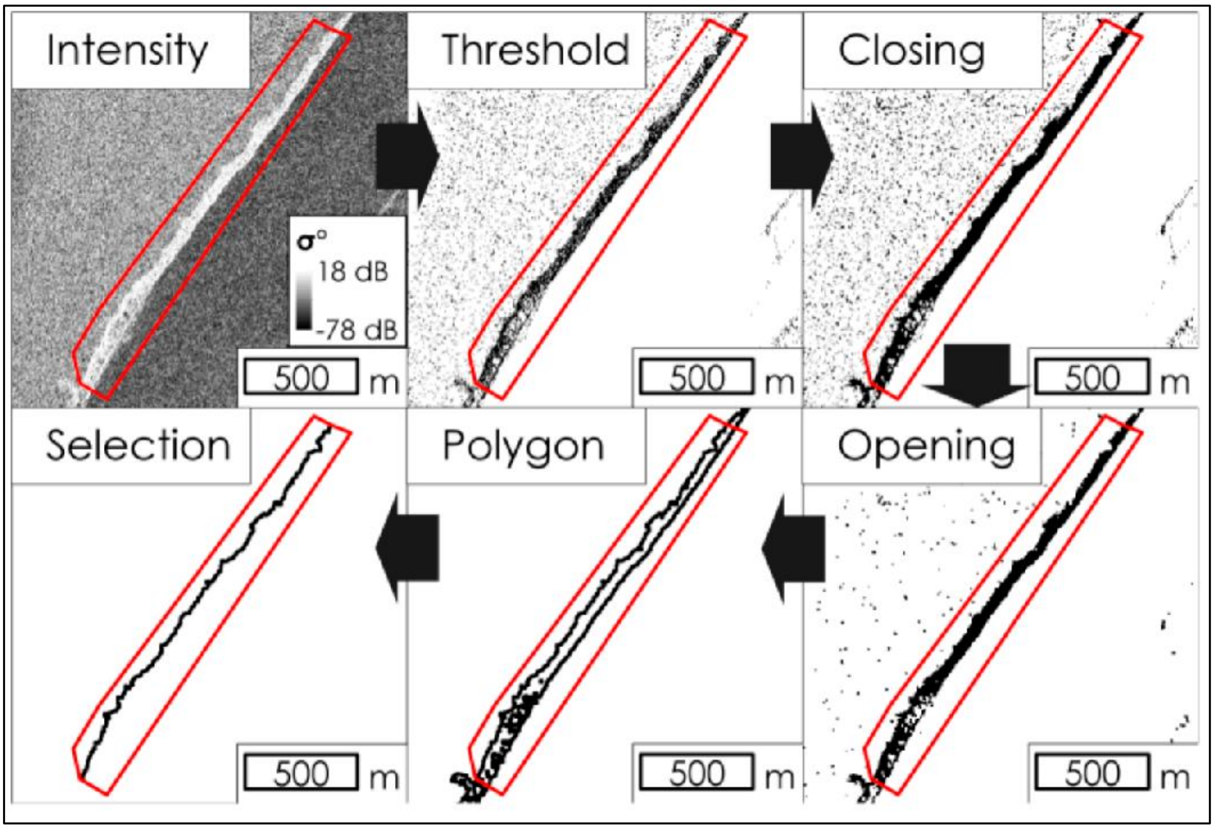

Figure 6 From Stettner et al. 2017: A Schematic of the automated approach to cliff-top line extraction outlining the relevant steps in the data processing. The first step is top left and follows through the path shown with the thick black arrows.

4.4 Implementation and adaptation of the thresholding approach for this study

The approach used by Stettner et al. (2017) requires modification to accommodate the lower resolution. The most important step towards implementing the approach described in Stettner et al. (2017) is the generation of the coastline boundary or line objects that accurately map out the land-water boundary in the Sentinel-1 data. To obtain line objects fitting this boundary more accurate and systematic and therefore also in a more comparable way than manually digitizing the coastline, a workflow was set up in ArcGIS with the modelbuilder tool. This tool enables setting up an automated processing chain in a flow chart format using a graphical interface, see Figure 7.Based on the approach from Stettner et al. (2017), a thresholding method is used where the classification target and filtering approach have been modified for the c-band data. The area is here classified in a binary manner into land area on the island and water or sea area surrounding it in a binary classification. Further differentiating the cliff face from the flat land as well as the water as done by

Stettner et al. (2017), with TerraSAR-X data is not feasible with the low-resolution C-band Sentinel-1 data.

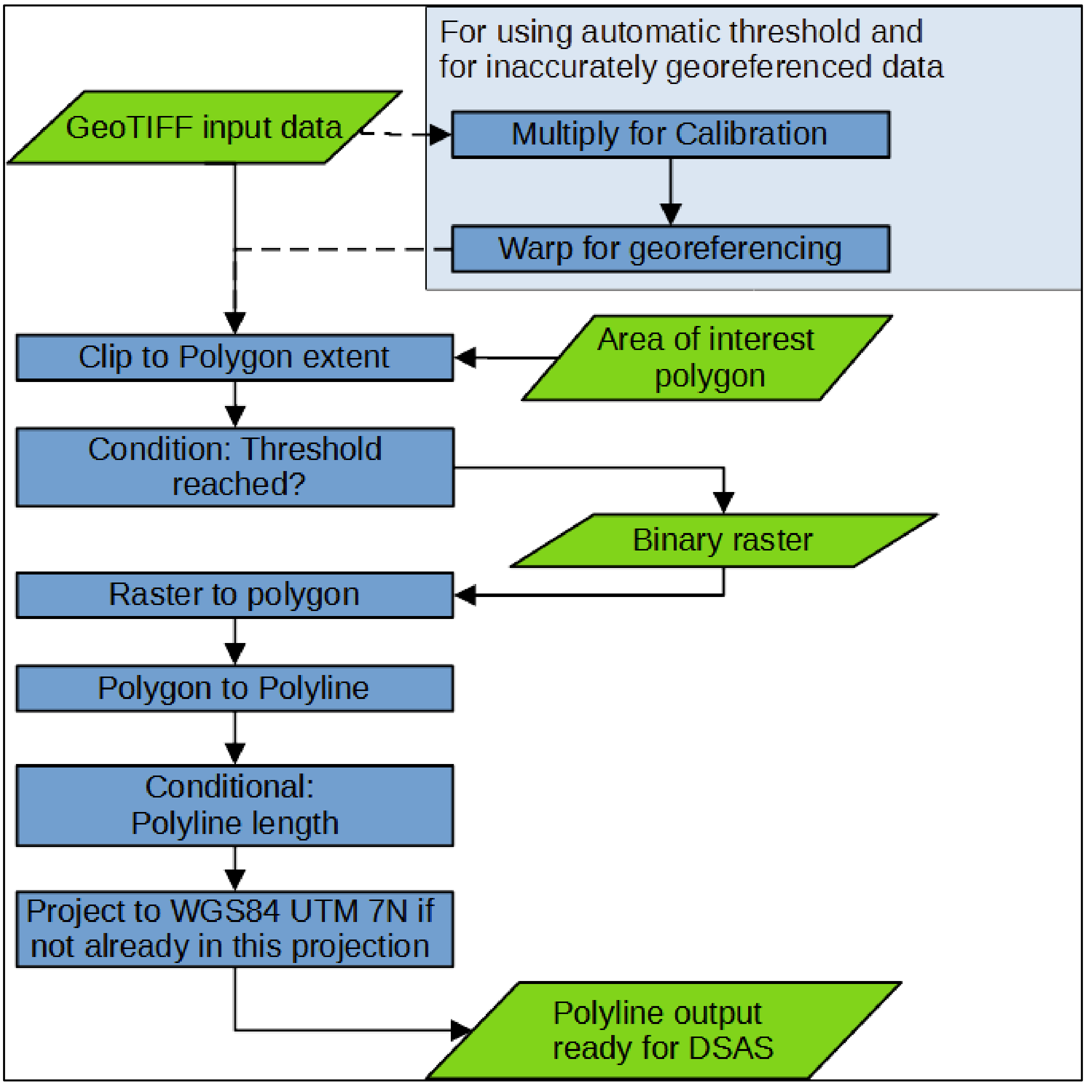

Figure 7 ArcGIS processing chain flowchart describing the thresholding method used in this study. Beginning with the raster input, the coastline is mapped as a line object.

The next step is to filter out the misclassified pixels and clusters of these resulting from the irregular Backscatter values that are spread in effectively random way around the image due to the speckle effect. Smoothing the result with e.g., a morphological filter, as described in Stettner et al. (2017) is not a viable solution as this leads to changes of mapped area on the scale of multiple pixels, which are significantly larger than for the TerraSAR-X data used there. This would result in larger than permissible uncertainties in the coastline position to contribute towards an accurate and reliable estimate of the erosion rate. Initially an approach was used which first assigned a size to the clusters of pixels classified with the 0 and 1 values. A selection based on polygon area size was attempted but resulted in removal of portions of the coastline from the polygon object as well as failing to produce the results reliably. Especially for areas without a clear intensity boundary with very variable intensity between adjacent pixels ware affected by this. This presented a problem, as these stretches are most commonly are classified in separate clusters or patches of pixels. Instead of a filter based on polygon size, the polyline length threshold was a better filter to remove only small pixel clusters but not the complex coastline. This selection simply removes smaller clusters, as the pixel clusters from the speckle effect have a small side length. The more complex clusters from incompletely classified coastline are not removed due to their more complex structure and larger side length of the polygons resulting from this morphology.

Having attempted to clean the raster as best as can be managed with this simple filter, the next step in the processing is the digitization or conversion to line objects to perform spatial measurements on. The data is converted in two steps first to polygon and then to line features, as the data must be in polyline format as an input to DSAS, which is used to calculate distances and erosion rates. To remove the small clusters of pixels from these line layers, the selection based on line-object length is performed before reprojection and output to the Geodatabase. Once the lines representing the coastline at the times of observation have been generated and projected to WGS 1984, UTM zone 7 North, they contain only the coastline and other larger features such as a small feature which is likely a lake of 400m diameter. As in Stettner et al. (2017) the DSAS [v 4.0] extension is used to calculate erosion rates and statistics; with MS Excel then subsequently used to generate further statistics and visualise the results.

Different principles can be applied depending on choice of threshold value. The threshold value is visually chosen to best represent the boundary between high-intensity land area and low intensity water area. The threshold value must lie between the mean of these two types of areas. It is chosen by the criterion of least surface length of the polyline object representing the position of the coastline. This means the straightest or cleanest line result is preferred which contains the least loops deviating away from the visible coastline resulting from randomly lower or higher intensity in clusters of pixels. The second criterion is the choice of threshold which places the coastline at the highest gradient in the Backscatter intensity. For the automatic threshold determination there are two simple options: a reference dataset and threshold can be selected based on the visual choice of threshold and the other images scaled to the distribution of σ_0 values from the reference dataset. The other simple option would be a simple statistical evaluation of the distribution, calculating the threshold value to represent the local minimum in the values, see Figure 8 which would only work for summer observations based on the observations. This should be the value best separating the values into the σ_0 distributions for land and water surfaces.

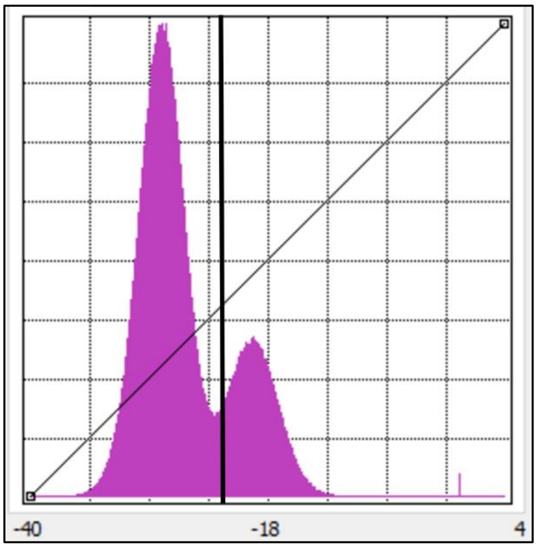

Figure 8 Backscatter intensity or σ_0-histogram for an entire scene in VV polarisation observed on ascending orbit observed on 08.07.2016 during summer as an example, also shown in Figure 30. The unmarked vertical axis shows pixel count with a maximum value of ≈35000, the horizontal axis values are given in decibels (dB).

4.5 Using Coherence thresholding to monitor coastline positions

The monitoring of coastal erosion using the Coherence between SAR scenes was considered a promising Approach when reviewing previous studies, see also Chapter 2. According to Short et al. (2011), high Coherence values were observed over the summer season considering data observed from multiple satellite systems - TerraSAR-X, RADARSAT-2 and ALOS-PALSAR. The suggestion was made to map large displacements between SAR acquisitions of Herschel Island by outlining the areas with Coherence loss in the high-resolution X-band data (from TerraSAR-X). The idea is that the eroded areas should exhibit low Coherence due to the large decorrelation of phase along with change in Backscatter. These areas and the water surface areas should then have a significantly lower Coherence value than the undisturbed land surface. The water surface is also expected to have low Coherence due to the decorrelation, which happens in seconds as the water surface level changes with wave action. Using the thresholding method to estimate the boundary between the areas with low and high Coherence should then give a good estimate of the coastline position between each year. The observations from the winter season are not expected to be usable for this purpose. The reason being the high coherency of stable coast-bound ice, which may be present for over half of a year. The sentinel-1 C-Band data is expected to be useable for Coherence between years: Year-to-year interferograms could not be formed from the X-Band TerraSAR-X data, but for C- and L-band this was successful, Short et al. (2011). Due to the low vegetation and otherwise largely only seasonally changing surface, the land surface area is expected to show high Coherence also between years, particularly during the summer season. The coastal area with ongoing erosion is expected to be decorrelated but have noise in the decorrelated area due to the low resolution inherent in the c-band data. This is exacerbated by the moving window in which Coherence is estimated, which lowers the resolution.

Another step may be to take advantage of having relatively dense (repeat-pass time: 12d) observations to improve the data quality: Stacking multiple Coherence datasets generated from successive observations, e.g., from within the summer season, could provide a yearly estimate of the coastline positions. C-band InSAR data is expected to be reliable for at least this time interval, as Interferograms could be generated for up to 4 years between datasets, Yonezawa & Takeuchi, (2000).

Based on the information and assumptions, the following approach is used in this study: The coherency between multiple datasets observed in the summer season between July and October from each year is estimated. Each coherency estimate is made between two datasets observed 12 days from each other (or from the next closest available dataset based on observation time). This is repeated for each set of two observations within each year. The resulting coherency estimates are then stacked within each year from 2016 to 2020.

4.6 Coherence estimation processing

The estimation of Coherence between SAR scenes is performed by a processing chain or flowchart model graph, as illustrated in Figure 9. The Coherence is estimated as the low-lag cross-correlation of complex-valued pixels. Mathematically it is expressed as *Equation (1)*, Bickel (2017), which is an estimate of the sample Coherence $\hat{\mu}$. In practice, the sample Coherence is calculated in a 5 × 2-pixel window (range & azimuth size). The absolute value of the sum of the complex product of the pixels within the window (size indicated by n for any direction here) from one dataset with the complex conjugate of the other. This is divided by the magnitude of both autocorrelations.

$$|\hat{\mu}| \approx \frac{\left|\sum_{n=1}^{L-1} x_{1,n} x_{2,n}^{*}\right|}{\sqrt{\sum_{n-1}^{L-1} \left|x_{1,n}\right|^{2} \sum_{n-1}^{L-1} \left|x_{2,n}\right|^{2}}} \qquad (1)$$

Read The raw SLC datasets are read into the processing chain in parallel (actual computation may still be in series).

TOPSAR Split In this step, the sub swath(s) containing the study region from the SLC file acquired in Illuminating-Wide sensor mode is selected. The observations from this mode are performed in three subswaths, which is the main reason a Deburst operation should be performed, i.e., the antenna pattern removal to form a continuous image.

Apply orbit file Both scenes are assigned the precise orbital path from a file obtained from ESA's index of auxiliary data, see Bibliography. The precise orbital state vector files are automatically downloaded based on the time parameters in the metadata of the raw SLC files in SAFE format. If this fails, the files can be manually downloaded. This is also important to determine the baseline (or distance vector) between the observations, which is important for e.g., generating a DEM from the interferogram.

Back-Geocoding In this step the parts of each dataset that have now been selected for the AOI and assigned the precise orbital trajectories are precisely georeferenced with each other are read and then passed to the next operator. This assignment of multiple SAR scenes with sub-pixel accuracy (requiring interpolation to a common position grid) is termed Coregistration.

Interferogram This function computes the interferogram and Coherence estimate between two SAR scenes. The interferogram is calculate by complex conjugate cross-multiplication between the two images in a specific sliding window of pixels. The window size is set to two pixels in azimuth direction and 5 pixels in range direction due to the higher resolution in range direction. The Coherence is also computed based on this windows size by lag-free cross-correlation between the pixels of the scenes in the specified window size. This is the smallest window size that can be expected to yield significant Coherence values compared to the lower-valued (roughly 0< noise level <0.5) white noise when estimated on single-pixel basis.

TOPSAR Deburst In this step the antenna pattern is removed to make a continuous image from the

For the Coherence estimation, the Coherence is generated alongside the interferogram. The interferogram was not used further, the processing was simply set up this way due to stability issues and to reduce time setting the parameters (the optimization for using multiple input datasets appears to be low).

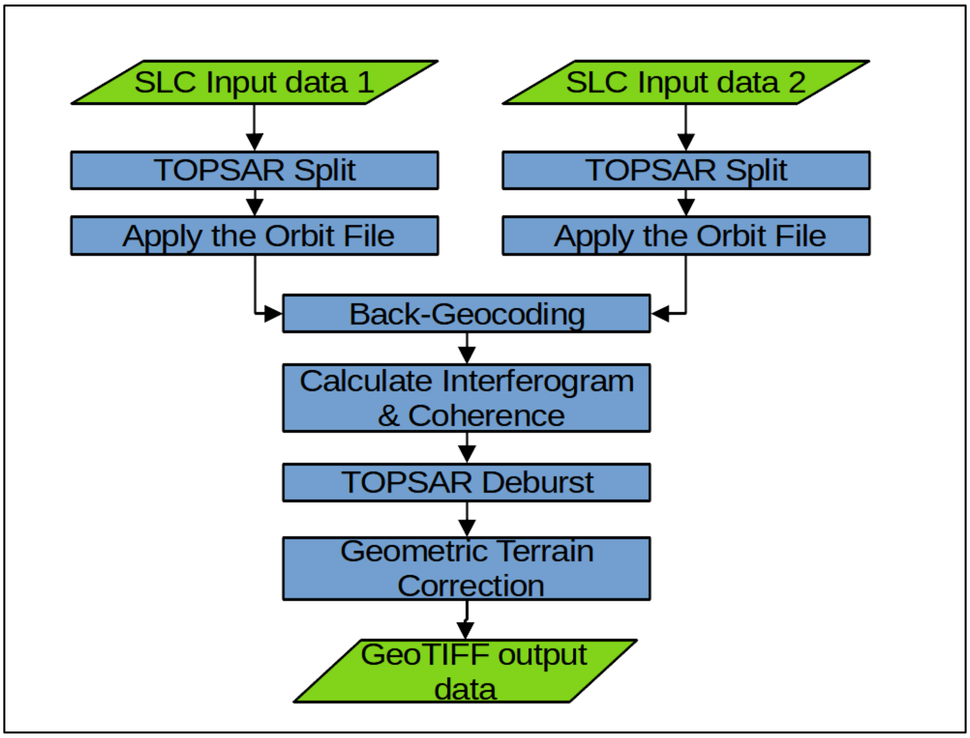

Figure 9 Processing flowchart to generate the Coherence between two SAR scenes.After generation of Interferogram with Coherence estimate from each GeoTIFF output the band containing the Coherence is stacked to generate a scene of average Coherence for each year. The Coherence band must selected with the BandSelect operator in SNAP or saved as layer in ArcGIS as the stacking is performed in ArcGIS as the addition operator used there does not have a selection setting.

4.7 Evaluation of results and predictions of future coastline position

The coastline positions are evaluated in excel, as this affords more ease and flexibility in calculation of specific parameters and their uncertainty level or confidence interval.

As the data itself is resampled to 5.86m by bilinear interpolation from 13.86m in azimuth and 3.86 in range direction for the Backscatter data with the processing steps applied, there is better resolution in E-W direction. In N-S direction there is smoothing due to the bilinear interpolation using a quadratic form for the interpolated values based on the sample location.

The uncertainty within the data is evaluated based on the estimated distribution of each time series of positions at each 5m along the baselines. This is described with the sample mean and standard deviation for each end-point rate, see Figure 13 to Figure 20. This represents the average and standard deviation assuming linear erosion rate between the positions for the first observation in time (2016 or 2017) and each subsequent position mapped with thresholding. The dates of each observation were simplified to decimal years to simplify the calculations in excel and obtain the accurate annual rates, as the observations are not from the same day of each year.

The future shoreline positions are based on the linear extrapolation to 5 years later than the last observed position, which is mid 2020 for both ascending and descending orbit-based data.

The linear trend in the data is fitted with the Excel SLOPE function, which is termed b in *Equation (2)* based on the correlation between x and y. The intercept used to calculate the fitted y is then simply calculated with the linear equation based on the mean x and y, see *Equation (3)*

$$b = \frac{\sum(x-\bar{x})(y-\bar{y})}{\sum(x-\bar{x})^2} \qquad (2)$$

$$a = \bar{y} - b\bar{x} \qquad (3)$$

The standard error for each time series of positions at each 5m along the baselines is calculated with the Excel STEYX function, which uses *Equation (4)*. The predicted y position represents the coastline position towards the landward side as a linear function of time as the x axis parameter.

$$\sqrt{\frac{1}{(n-2)}\left[\sum(y-\bar{y})^2 - \frac{[\sum(x-\bar{x})(y-\bar{y})]^2}{\sum(x-\bar{x})^2}\right]} \quad (4)$$

5 Results

5.1 Coastline positions mapped from Backscatter thresholding

The coastline positions based on thresholding of Backscatter data relative to the baseline have been measured for each of the three sites, see various subsets of the results in Figure 10**,** 11 and 12. The results describe the distance to the baseline along transect lines to the last intersection with the line objects representing threshold value boundaries generated by DSAS. The transects perpendicular to each baseline with a pacing of 5m; it should be noted that only for Site 2 the baseline is entirely straight. As the data and subsequent result quality of the coastline position from thresholding was significantly too low only data from the summer season (June-August for this subset of data) was used. The variance in the data from the winter season was too high to generate reliable results in 13 out of 14 cases. Conversely, only one of 10 datasets from the summer season could not be used, leaving 5 datasets observed on ascending and 4 datasets observed on descending orbit. Therefor 27 total lines are generated representing coastline positions across the three sites to measure and compare the efficacy of this mapping approach. Several manually digitized coastline positions have been made for Site 1 to gain an overview of realistic results from thresholding but are not strictly necessary. They are generally in agreement with the lines generated with this approach but have completely different structure see Figure 10.

5.2 Results generated using DSAS and prediction based on linear fit

The following results are smoothed by taking the 3-point moving average over each line of positions as generated by DSAS for every 5m along the baseline. This removes the step-like effect from the discrete pixels, as a smooth morphology better approximates real coastline structures (i.e., straight lines rarely observed in nature).

5.2.1 Results and predictions for Site 1: Cunliffe

The results for this site, see Figure 13 and Figure 14, are the clearest in the observed landward shift of the coastline over time. The position series shows that the coastal area is progressively and quickly eroding each year over most of the baseline, with the majority of the stretch having rates around 10m/yr. This appears to be continuous across almost all of Site 1, with the average value of the rate larger than its variation indicating reliable results. Little erosion or accumulation is only observed in the easternmost part of the site. The net change for 2016-2020 appears to be close to 40m over most of the coastal stretch of the study area based on data from ascending orbits, Figure 13, with most spike-like structures of variance in the net position change being from the 2020 positions. The data from descending orbits, Figure 14, also show large net coastline change, but not for the majority of the length of the study site as in Figure 13. The average erosion rate from this data (black line in Figure 14) is also shown as close to 10m/yr. for the majority of the stretch, with low rates or apparent accumulation at both ends.

The observations from ascending and descending orbits agree quite well for site 1, with the estimated erosion rate being close to the same with largely less than 0.3 m/yr. difference in rate at all points. The individual coastline position estimates for each year show more variance between the two looking directions for acquisition, which is also seen for different datasets from the same year from the same orbital direction. The fitted coastline positions for year 2020 also agree well with the 2020 observations for both sensor orientations, see Figure 15 andFigure 16. For the descending orbit data especially, the fitted and observed positions match very closely, see blue and upper black line in Figure 16. For the data from ascending orbits the fit between calculated and observed positions is mostly close as well, with larger differences from the variance in the 2020 observation, see blue and upper black line in Figure 15. Based on the predictions for the 2025 positions, there is statistically over 90% significant erosion over most of the length of the study site. Little or negative erosion is expected until 2025 in the prediction on the eastern part of the study site, as can be seen from the blue and red lines being within one margin of error from each other for many positions in the eastern side of the site. This is consistent for all data, see lines up to ≈ 150m along the baseline in Figure 15 andFigure 16.

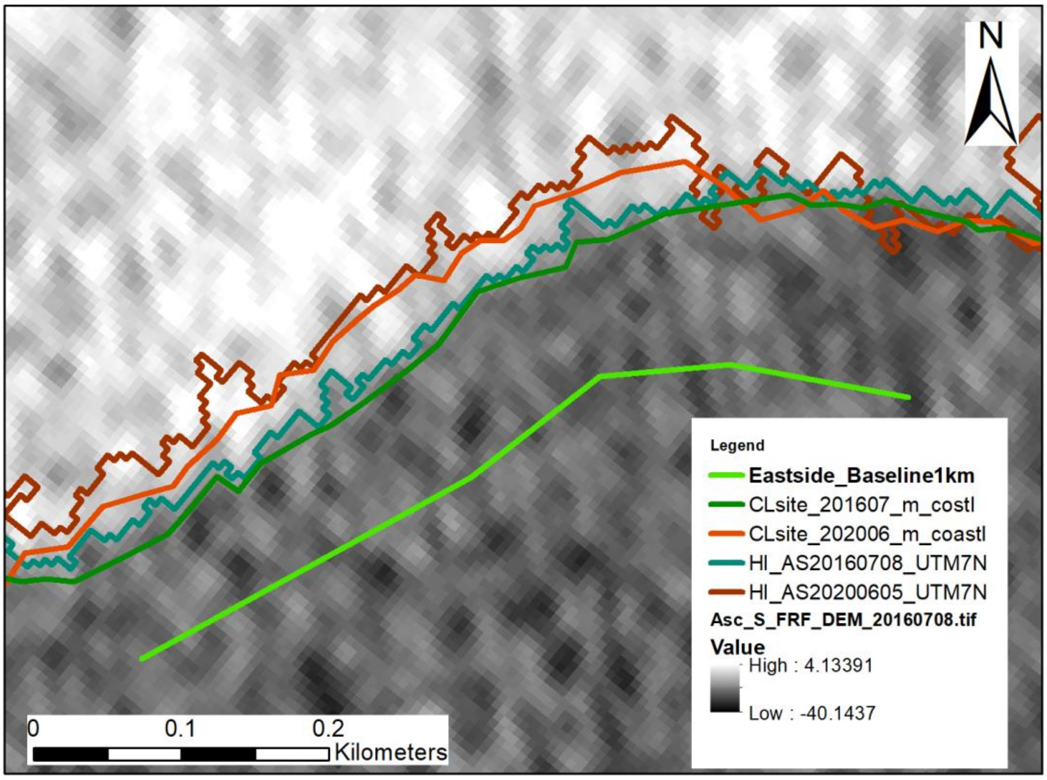

Figure 10 Site 1, Summer 2016 Two manually mapped coastline positions and two coastline positions generated with thresholding from Summer 2016 and June 2020 are displayed as coloured lines. In the background the SAR scene based on ascending orbit in dB in grayscale. The 2016 positions are the coarsely segmented darker green line for the manually mapped 2016 position. The blue line from the thresholding follows a step pattern as individual pixels are mapped. The same pattern occurs for the 2020 positions, orange line from manual digitization and reddish-brown line from thresholding.

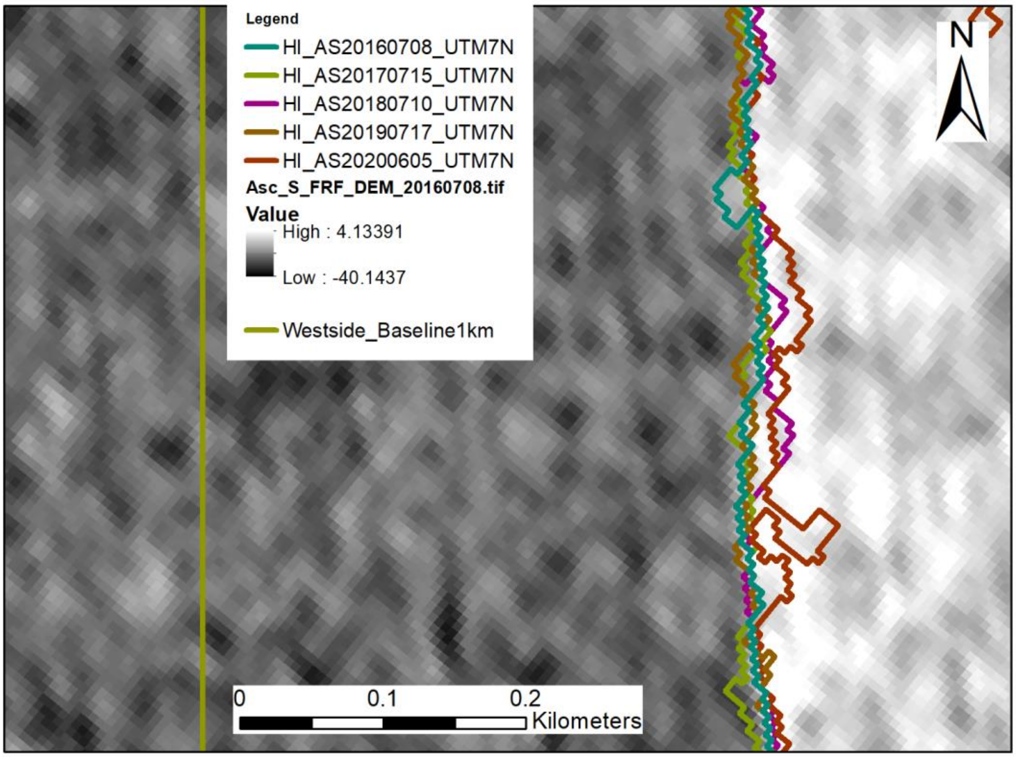

Figure 11 Site 2, Summer 2016: SAR Backscatter scene in dB observed from a descending orbit from in greyscale in the background with values in dB. Threshold lines representing coastline positions generated from data observed on ascending obits in the summer season for 2016 to 2020 marked in various colours shown East of the straight baseline (yellow-green line on the western part of the area).

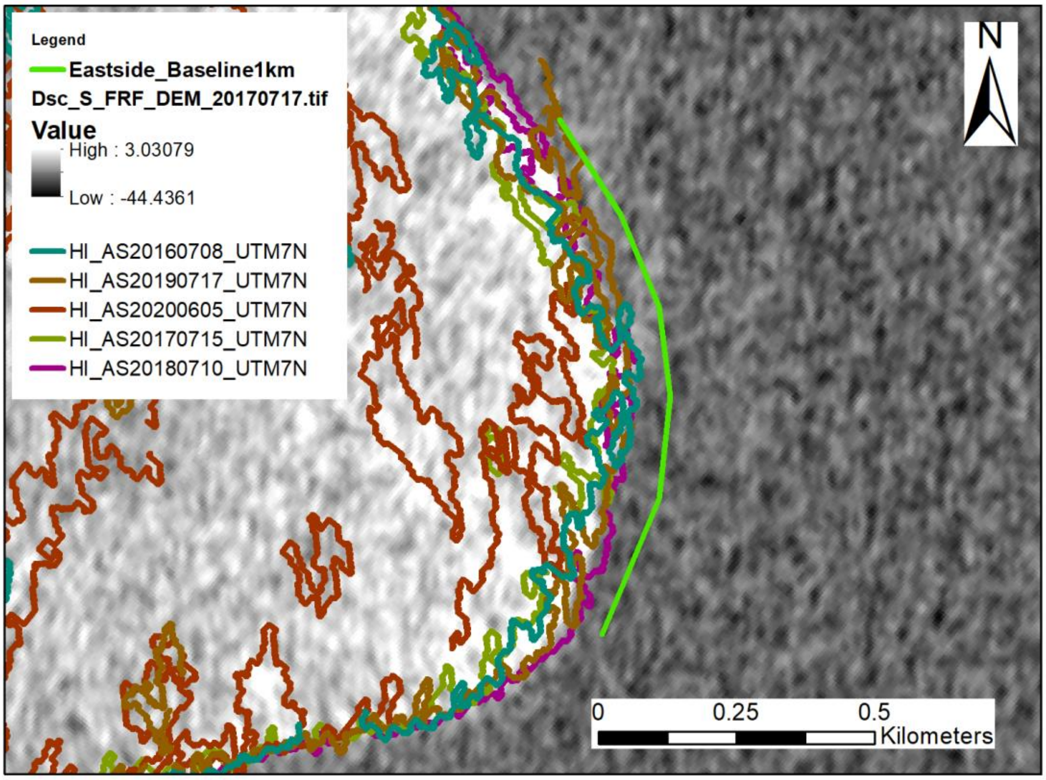

Figure 12 Site 3, Summer 2017 SAR Backscatter scene in dB observed from a descending orbit in greyscale in the background with values in dB. Threshold lines indicating coastline positions generated from data observed on ascending obits marked in various colours shown West of the curved baseline (green line) The high variance in the results and partially unsuccessful thresholding can be seen from the lines covering the surface further inland. This is the baseline for Site 3: Eastside, which is curved around the land surface to maintain similar orientation and distance to the coastline along its length.

5.2.2 Results for Site 2: Westside

For the data from Site 2 there is overall more small-scale variation in the results, with more oscillations around zero for the average erosion rate based on the changes to the first position observation, observable for both sensor orientations in Figure 17 and Figure 40. The variation (standard deviation) in the average annual erosion is much greater for the data observed on descending orbits for Site 2, which is due to the 2018 coastline position being an outlier, see purple line in Figure 40. There appears to be no significant average erosion rate result from the Site 2 data, as for all datasets the average rate is close to zero with high variance.

The predictions for both ascending and descending orbits for the June and July 2025 positions respectively are largely not different from with 90% confidence, indicating very low erosion rates at this site. The fitted linear erosion rate is largely positive for data from ascending orbits and negative for data from descending orbits, see Figure 18 andFigure 41. This indicates that the estimates are not reliable and is in accord with the overall apparently low erosion rate at this site compared to Site 1.

5.2.3 Results for Site 3: Eastside

For this site, the results from ascending orbits, looking eastwards, show the greatest variance and errors, see incomplete coastline positions in Figure 42. The variance in erosion rate estimates from this data is much larger than the estimated average rates, making this data unusable, which leads to the exclusion of this result from the overall averages, see

Table 1. Along the baseline of Site 3 there are many points where the Backscatter intensity in data acquired looking eastwards was not significantly higher on land than for the water, leading to missing position values. The data acquired looking westwards (descending orbit) towards the coastline yielded much more accurate and complete results; compare the much smaller standard deviation in the erosion rates, see green error bars in Figure 19 compared to Figure 42. The positions are grouped much tighter together and are shown on a smaller vertical range on Figure 19 compared to data looking eastwards on an ascending orbit shown in Figure 42. The data acquired on descending orbits shows a clear erosion trend, with the last observation form 2020 most landwards, see orange line in Figure 19. The average and linear fitted erosion rates are smaller here based on data from descending orbits, around half of the values from site 1.

The predictions for the 2020 and 2025 positions from data from ascending orbits is not significant with 90% confidence; the estimated positions are even outside of the plotted range in Figure 43. The predicted 2020 and 2025 coastline positions based on data acquired on descending orbits appears much more believable, with these estimates being close to one 90% confidence interval apart from each other for most of the stretch. In some places also more than one conf. interval apart from each other, see blue and red curved with error bars in Figure 20. Here the predicted 2020 coastline position (upper black line in Figure 20) matches up for most of the points to within 5m. This indicates that there is a lower, yet reliably determinable rate of erosion at Site 3.

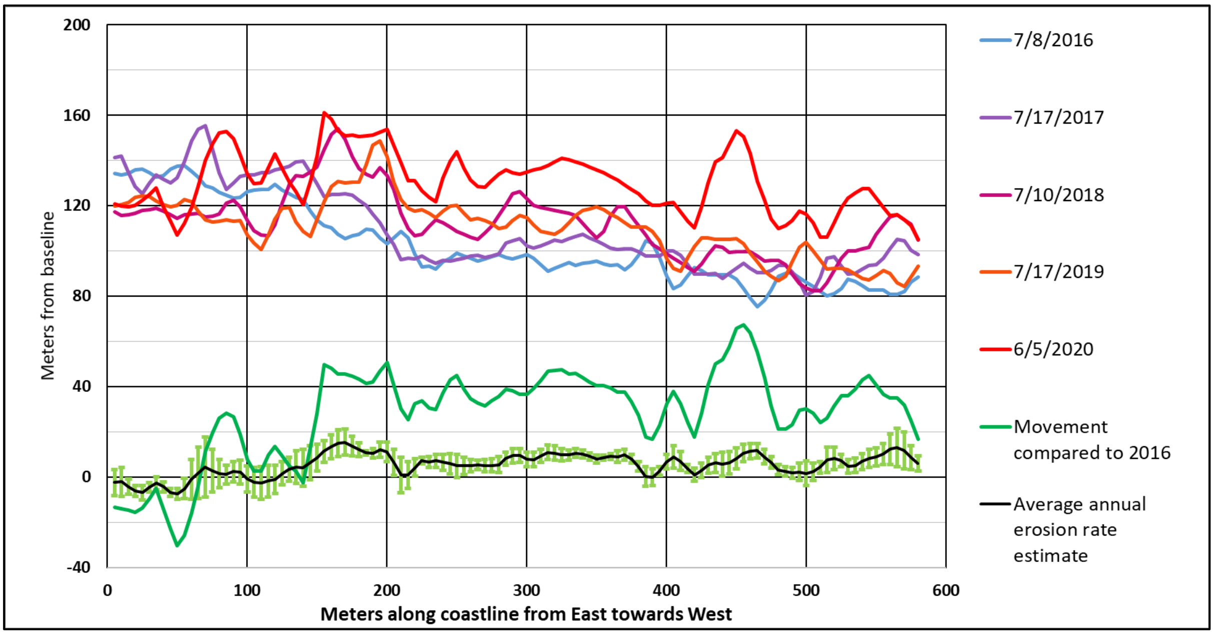

Figure 13 Site 1 - Cunliffe: data observed on an ascending orbit. The blue, purple and red lines show the coastline positions relative to the baseline, with the land side above the lines. The black line represents the average erosion rates when comparing each year to the first position from 2016 Positive values represent erosion, negative values represent coastline progradation seawards by accumulation of sediments. The standard deviation of these values is given around the curve as green error bars. The darker green line shows the distance and direction of change in position between the first observed position from 2016 and the last observed position from 2020 along the Site 1 baseline. The point spacing along the baseline is 5m, with 116 values plotted on each line. The vertical axis positive direction is North to North-West.

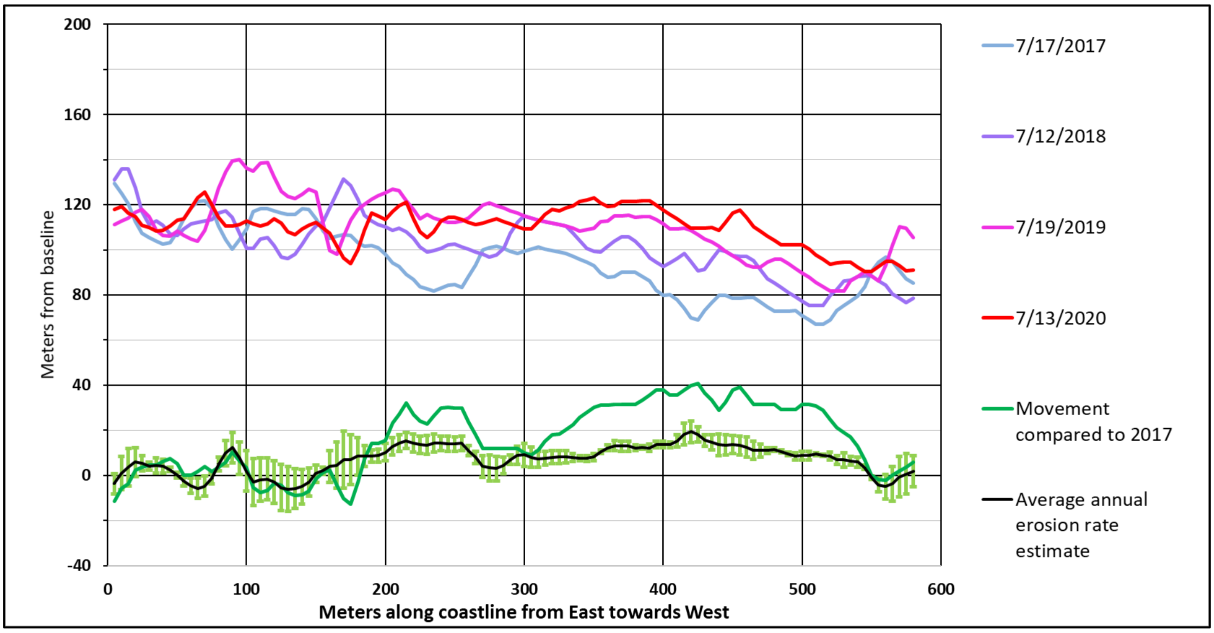

Figure 14 Site 1 - Cunliffe: data observed on a descending orbit. The blue, purple and red lines show the coastline positions relative to the baseline, with the land side above the lines. The black line represents the average erosion rates when comparing each year to the first position from 2017. Positive values represent erosion, negative values represent coastline progradation seawards by accumulation of sediments. The standard deviation of these values is given around the curve as green error bars. The darker green line shows the distance and direction of change in position between the first observed position from 2017 and the last observed position from 2020 along the Site 1 baseline. The point spacing along the baseline is 5m, with 116 values plotted on each line. The vertical axis positive direction is North to North-West.

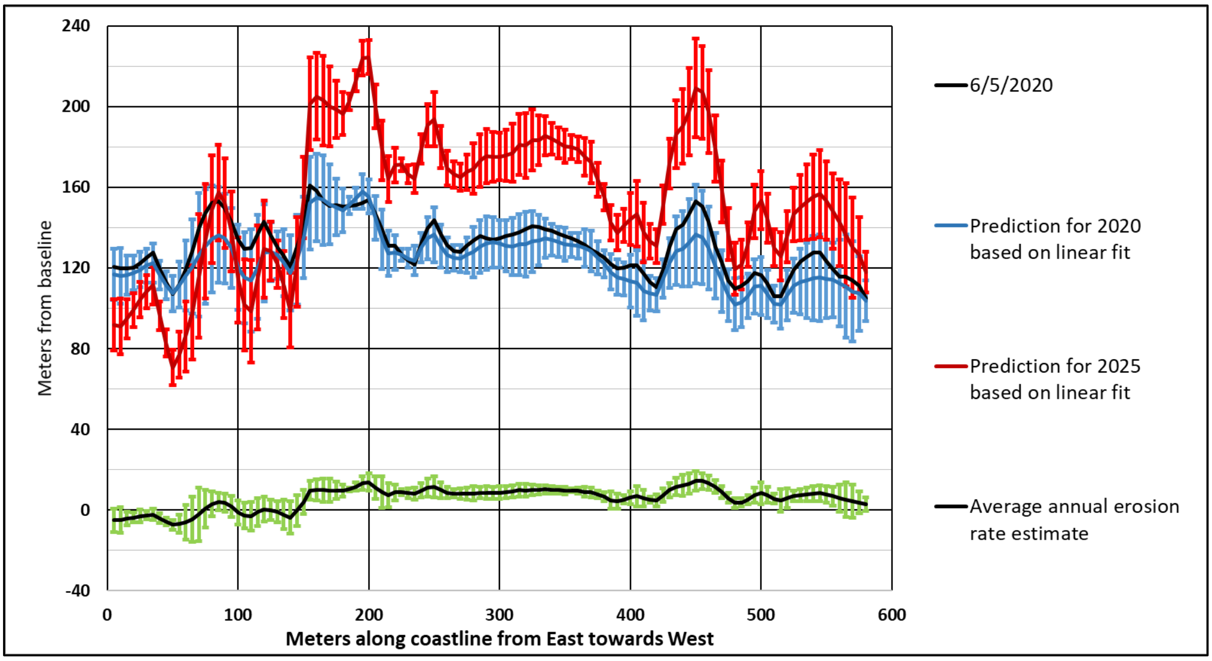

Figure 15 Site 1 - Cunliffe: prediction of coastline positions based on data observed on an ascending orbit; landward side above lines. The black curve at the middle or top shows the observed coastline position for 05 June 2020 with the predicted position assuming a linear erosion rate as a blue line. The blue error bars show the two-sided 90% confidence interval around the blue line which was calculated the t-test margin of error. The predicted June 2025 coastline position is shown with the red line with the same margin of error. The rate of change based on a linear fit of the data displayed as the black line at the bottom of the figure. The standard deviation of average rate of change compared to the first value from 2016 is marked around this line as green error bars. The point spacing along the baseline is 5m, with 201 values plotted on each line. The vertical axis positive direction is North to North-West.

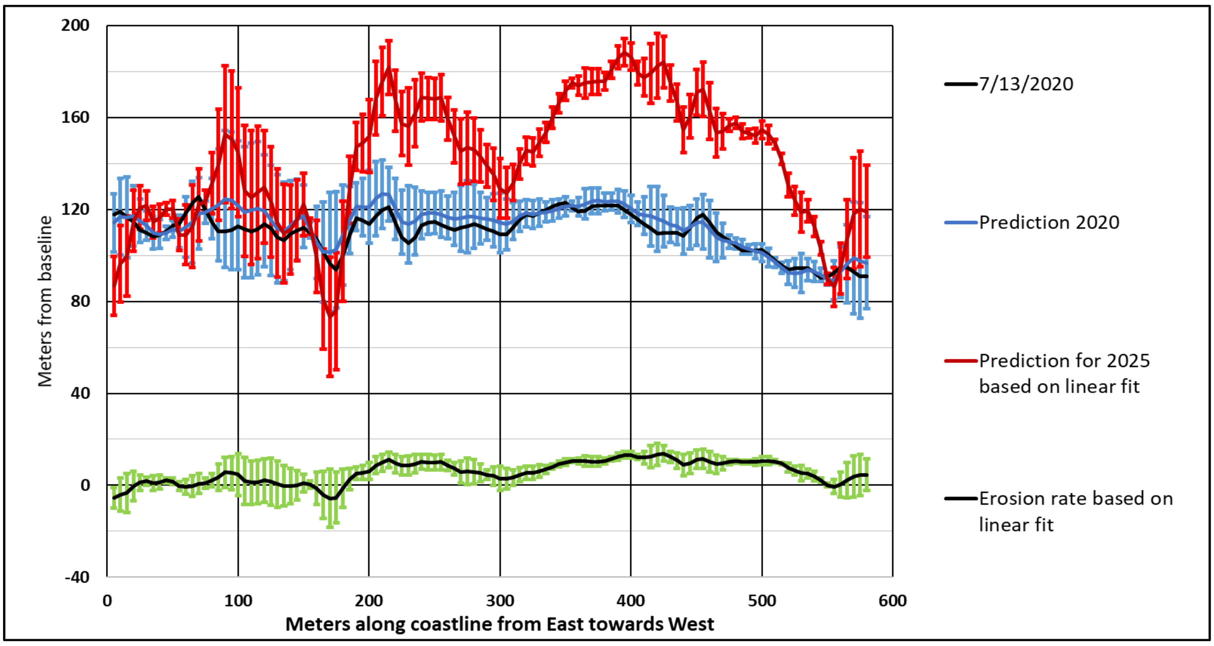

Figure 16 Site 1 - Cunliffe: prediction of coastline positions based on data observed a descending orbit; landward side above lines. The black curve at the middle or top shows the observed coastline position for 13 July 2020 with the predicted position assuming a linear erosion rate as a blue line. The blue error bars show the two-sided 90% confidence interval around the blue line which was calculated the t-test margin of error. The predicted July 2025 coastline position is shown with the red line with the same margin of error. The rate of change based on a linear fit of the data displayed as the black line at the bottom of the figure. The standard deviation of average rate of change compared to the first value from 2016 is marked around this line as green error bars. The point spacing along the baseline is 5m, with 201 values plotted on each line. The vertical axis positive direction is North to North-West.

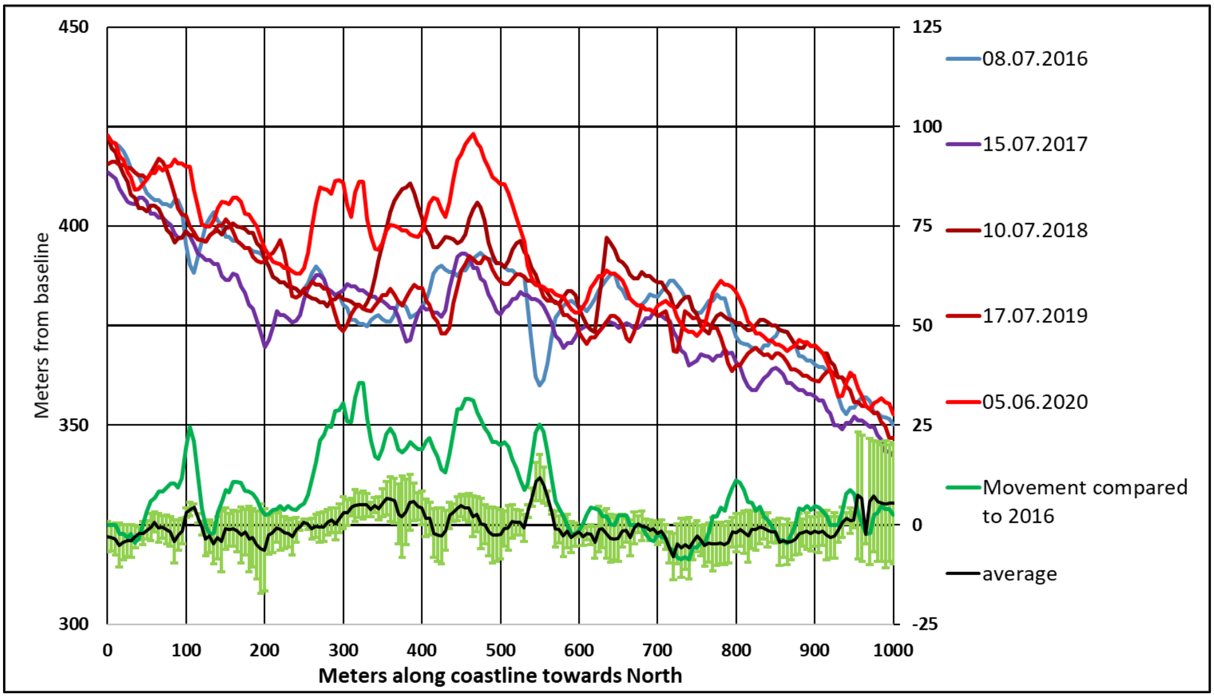

Figure 17 Site 2 – Westside: data observed on an ascending orbit. The blue, purple and red lines (left vertical axis) show the coastline positions relative to the baseline, with the land side above the lines. On the right vertical axis (same scale but with an offset) is the black line representing the average erosion rates when comparing each year to the first position from 2016. Positive values represent erosion, negative values represent coastline progradation seawards by accumulation of sediments. The standard deviation of these values is given around the curve as green error bars. The darker green line (right vertical axis) shows the distance and direction of change in position between the first observed position from 2016 and the last observed position from 2020 along the Site 2 baseline. The point spacing along the baseline is 5m, with 201 values plotted on each line. The vertical axis positive direction is East.

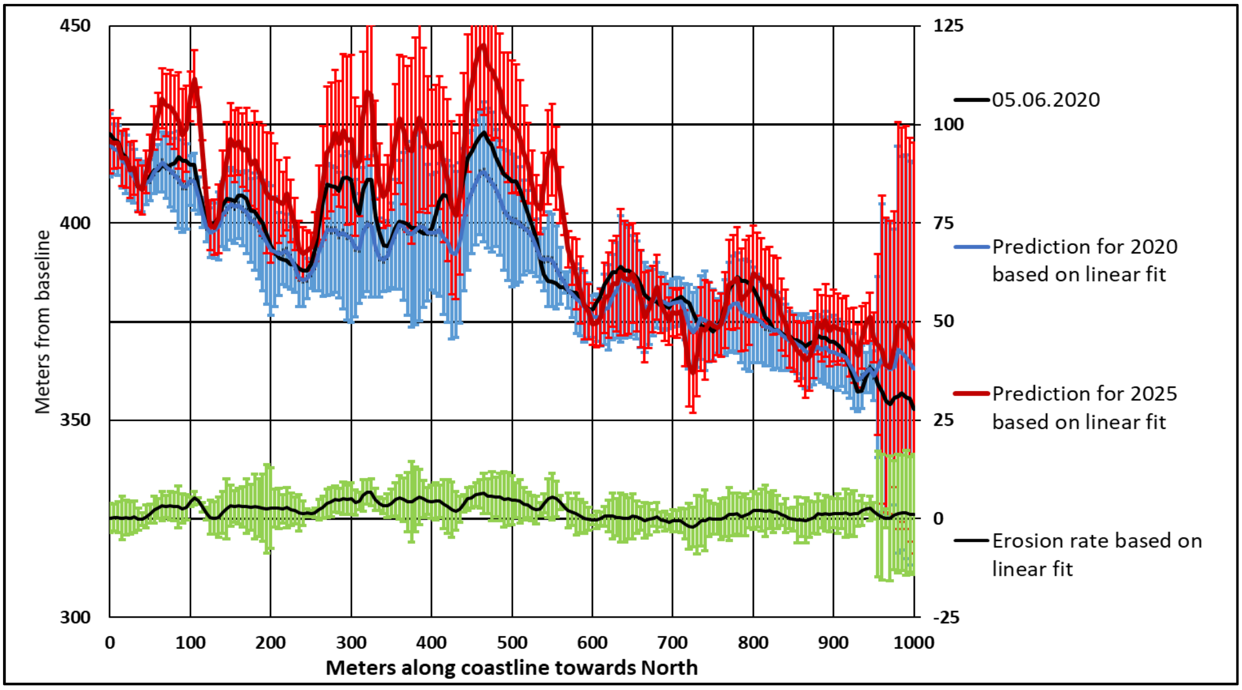

Figure 18 Site 2 – Westside: prediction of coastline positions based on data observed on ascending orbit; landward side above lines. The thicker black curve at the middle or top shows the observed coastline position for 05 June 2020 (left vertical axis) with the predicted position assuming a linear erosion rate as a blue line. The blue error bars show the two-sided 90% confidence interval around the blue line which was calculated the t-test margin of error. The predicted June 2025 coastline position is shown with the red line (left vertical axis) with the same margin of error. On the right vertical axis (same scale but with an offset) is the rate of change based on a linear fit of the data displayed as the black line at the bottom of the figure. The standard deviation of average rate of change compared to the first value from 2016 is marked around this line as green error bars. The point spacing along the baseline is 5m, with 201 values plotted on each line. The vertical axis

positive direction is East.

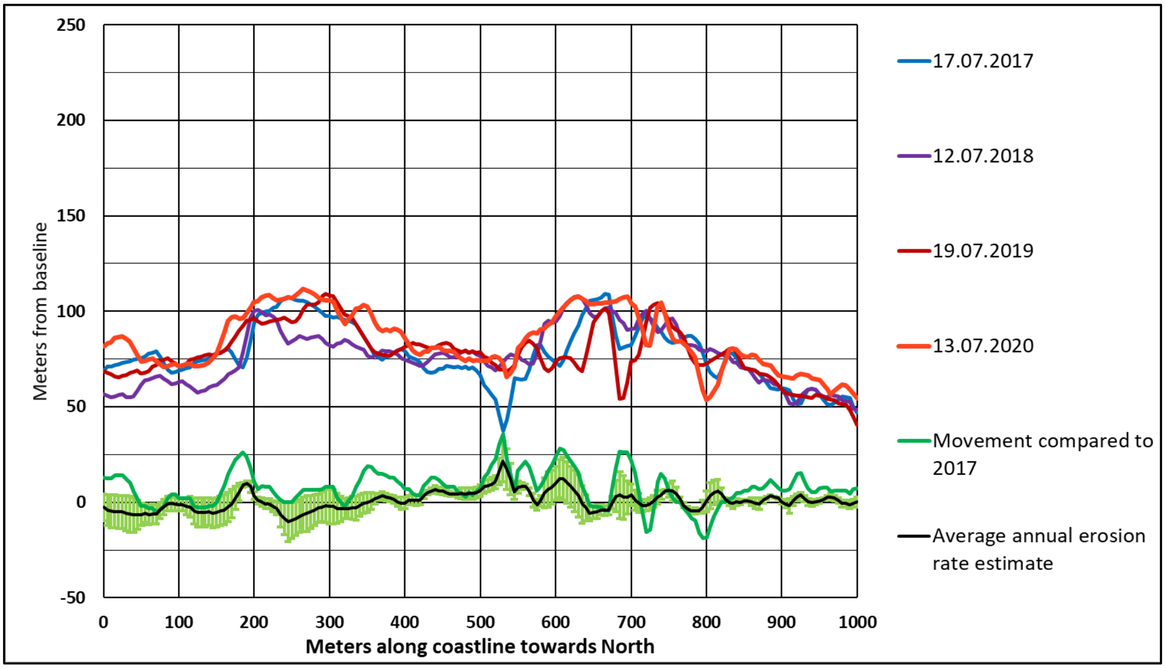

Figure 19 Site 3 – Eastside: data observed on a descending orbit. The blue, purple and red lines show the coastline positions relative to the baseline, with the land side above the lines. The black line represents the average erosion rates when comparing each year to the first position from 2017. Positive values represent erosion, negative values represent coastline progradation seawards by accumulation of sediments. The standard deviation of these values is given around the curve as green error bars. The darker green line shows the distance and direction of change in position between the first observed position from 2017 and the last observed position from 2020 along the Site 2 baseline. The point spacing along the baseline is 5m, with 201 values plotted on each line. The vertical axis positive direction is North-West (left side of plot) to South-West (right side of plot) due to curved baseline.

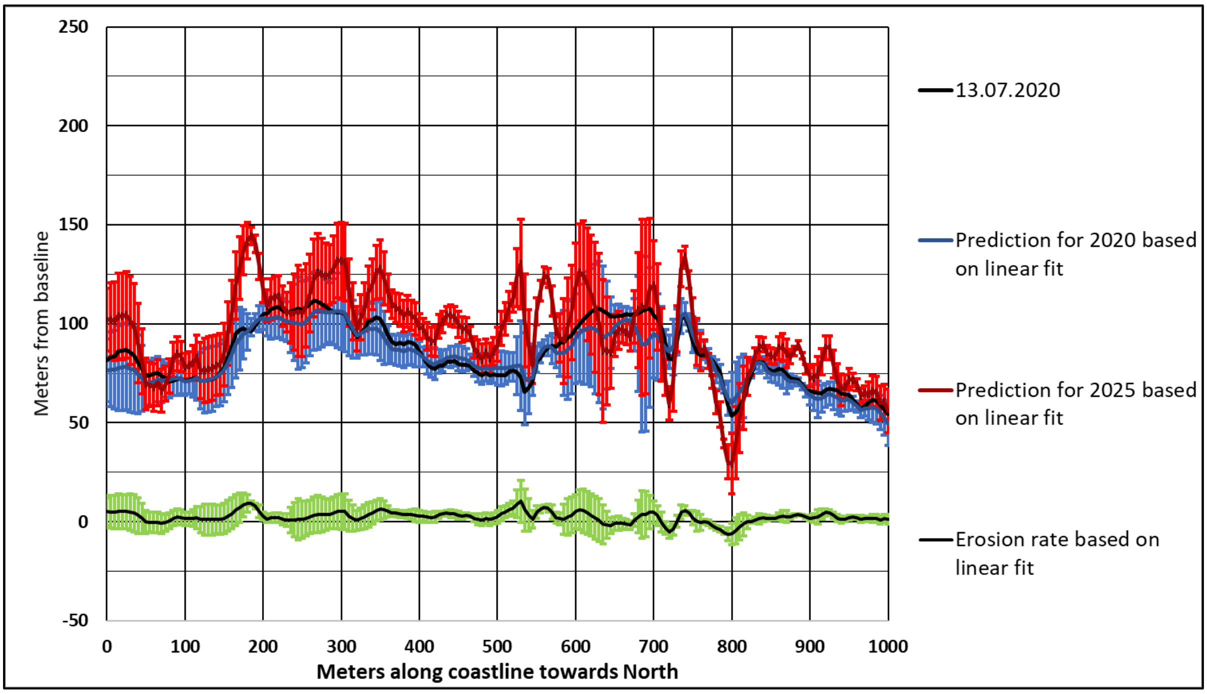

Figure 20 Site 3 – Eastside: prediction of coastline positions based on data observed a descending orbit; landward side above lines. The black curve at the middle or top shows the observed coastline position for 13 July 2020 with the predicted position assuming a linear erosion rate as a blue line. The blue error bars show the two-sided 90% confidence interval around the blue line which was calculated the t-test margin of error. The predicted July 2025 coastline position is shown with the red line with the same margin of error. The rate of change based on a linear fit of the data displayed as the black line at the bottom of the figure. The standard deviation of average rate of change compared to the first value from 2016 is marked around this line as green error bars. The point spacing along the baseline is 5m, with 201 values plotted on each

line. The vertical axis positive direction is North-West (left side of plot) to South-West (right side of plot) due to curved baseline.

5.2.4 Summary of results from the three sites

Table 1 Results for total erosion and annual rate estimates with uncertainties from the three sample sites and expected total annual area loss on Herschel Island based on these values

Result		**Unit**	**Site 1: Cunliffe site**	**Site 2: Westside**	**Site 3: Eastside**
Ascending - time interval 2016-2020	Average movement of coastline over time interval based on linear fit	m	28.4	9.2	31.6
	Average 1-sided 90% confidence interval	±m	14.1	12.6	70.5
	Annual erosion rate based on linear fit	m/yr.	7.1	2.3	7.9
	Standard deviation in annual erosion rate	±m	4.1	4.7	22.9
	Estimated annual area loss on Herschel Island	km²	1.2	-0.1	1.1
	Total estimated net area change along baseline	m²	12371	-1564	18412
	Uncertainty in estimated net area change	±m²	2401	4751	22985
Descending - time interval 2017-2020	Total estimated net area change along baseline	m²	12201	10113	2058
	Uncertainty in estimated net area change	±m²	2353	8236	4551
	Average movement of coastline over time interval based on linear fit	m	18.7	11.9	9.1
	Average 1-sided 90% confidence interval	±m	11.6	18.6	12.0
	Annual erosion rate based on linear fit	m/yr.	6.2	4.0	3.0
	Standard deviation in annual erosion rate	±m	4.1	8.2	4.5
Overall Average 2016-2020 excluding Site 2: Descending and Site 3: Ascending values	Estimated total area loss on Herschel Island	km²	1.2	0.6	0.1
	Annual average erosion rate based on linear fit	m/yr.	**4.7**		
	Standard deviation or spread of annual erosion rates from all three sites	m/yr.	**4.4**		
	Standard deviation or uncertainty in annual erosion rates	m/yr.	**4.4**		
	Estimated average annual area loss on Herschel Island	km²/yr.	**0.4**		

The aggregated results based on sensor looking direction and individual study site are listed in

Table 1. The overall averaged results based on the results from each study site have been calculated. This was performed while excluding values where the margin of error was close to twice the size of the average observed movement over the 4 or 5 years, respectively. This was the case where the sensor looking direction was seawards relative to study Site 2 and 3. The sensor looking direction is East on an ascending orbit with flight trajectory towards North and West on a descending orbit with flight trajectory towards South. Site 1 is largely parallel or within 30° of the looking direction for both orbital directions. There is little difference in the results from the two orbital directions for Site 1 as opposed to the results from Site 2 and Site 3. This is already obvious from the data, see the similarity between Figure 13 and Figure 14compared to the large differences between Figure 17 and Figure 40 as well as Figure 42 and Figure 19.

5.3 Seasonality in the scenes and results

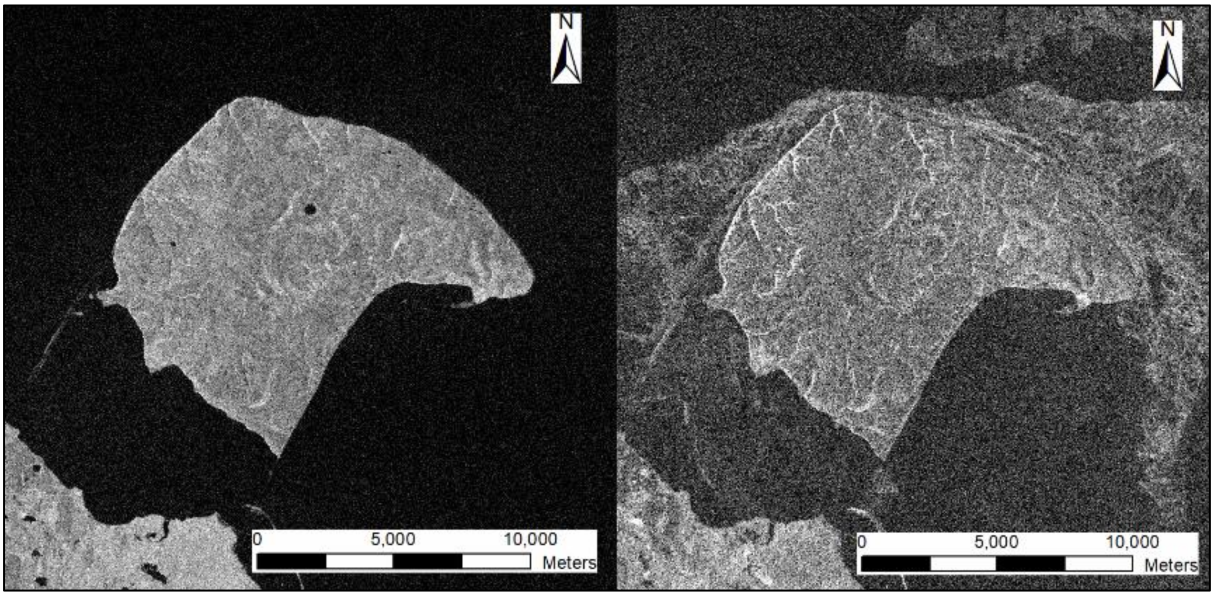

Figure 21 The two SAR scenes here display the Herschel Island target. The scene on the left was captured in July 2016 and the scene on the right in April 2016, just over three months before. This data was acquired on an ascending orbit with sensor looking towards East.

One key question towards using C-band SAR data to monitor coastal retreat with the approach described in Stettner et al. (2017) is the viability of delineating the coastline from data acquired during different seasons. There is significant seasonality observable in the SAR data, which is mainly due to the variable ice and snow cover and ground freezing on land and sea. The ground area itself freezes and thaws seasonally as it itself consists partly of ice and contains larger ice structures as indicated in the introduction Chapter of this text. There may also be a thick(er) snow cover during the winter which reduces the Backscatter intensity compared to bare ground, Buchelt et al. (2021). The sea area shows thinner patches of ice cover that have a relatively high average Backscatter value in the winter season, with snow cover only on the sea ice. The Backscatter intensity of the sea ice is closer to the average of the land area than the open water, see right scene in Figure 21. These patches of ice are interspersed with larger blocks of ice which exhibit a lower Backscatter intensity, more similar to the intensity of the open water. From the whitish-appearing area around the island on the right side of Figure 21 it is apparent that the sea-ice cover is only partial. An observation date during which a full sea-ice cover is present is not encountered in the data since 2014 but is expected generally during the winter season for this region. It is expected that the Backscatter characteristics on the land area and other factors such as direction of looking with the sensor play an important role here in determining which areas may be accurately mapped. This large effect is partly expected due to selection of data such that the time of acquisition coincides with the time of year with little to no sea ice in the summer and with greatest sea-ice cover towards the end of winter.

5.4 Comparing Backscatter thresholding results with drone imagery

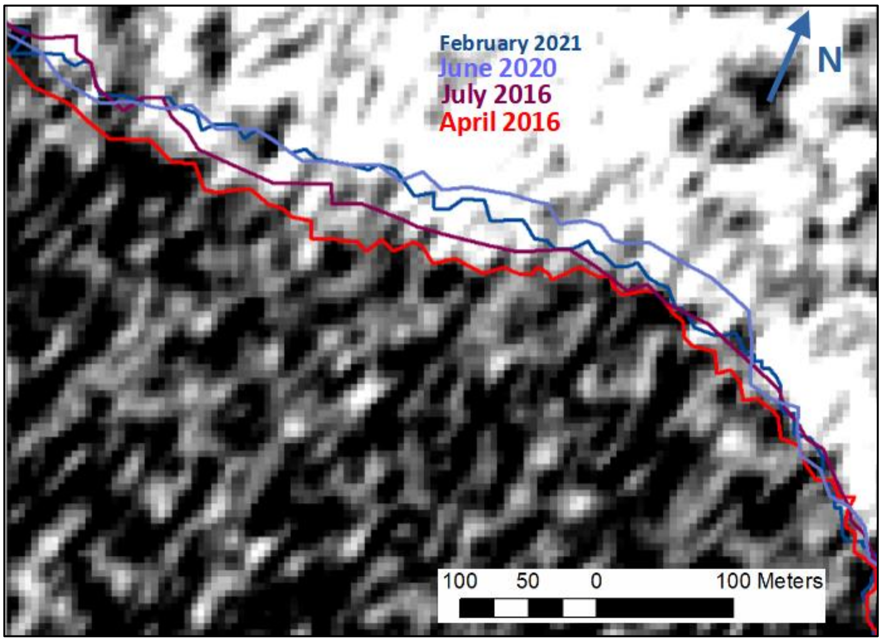

Figure 22 Manual digitization of coastline based on SAR scene from date, corresponding to colour in list in lower middle part of the figure. SAR scene in black and white from April 2016 in background. The image is rotated due to a change of projection, see North arrow. This data was acquired on an ascending orbit with sensor looking towards East, showing part of the scene in Figure 21.

The SAR scene shown in Figure 22 shows Site 1, a small area of the coastline on the South-Eastern side of Herschel Island. This Scene shows the Backscatter intensity from the single observation on 15th of April 2016. The greyscale colour has been scaled so that the difference between the land and water area is more apparent. This step is necessary to improve the visual differentiation due to the colour scaling, which is automatically adjusted to a statistical measure of the colours in the image such as percentiles. Figure 22 shows the visually evaluated position of the coastline at four different times. The lines were constructed by drawing a line between the seaward lying corner vertices of the areas of pixels at or above a certain brightness level which represents the higher Backscatter observed on the land area. As can be seen in Figure 44 and Figure 22.

The manually mapped coastline positions, see Figure 22and Figure 24, do agree well with the position of the shoreline or cliff-top line clearly visible in Figure 24 from the drone imagery for July 2016. The mismatch in position is only of the order of 10m compared to the coastline position mapped from the SAR scene for the same month (July 2016). The results obtained with the simple thresholding method are significantly more reliable than with manual mapping, given sufficient data quality. An important prerequisite here was the more accurate georeferencing during the terrain-correction with a Digital Surface Model (DSM) generated from ALOS SAR data, see Tadono et al. (2014). This improves the geo-referencing accuracy to the pixel level at ≈5m. This was evaluated visually by comparing various features across the entire scene, where no parts of the image appear to have any significant spatial shift at many recognisable features including many areas with clear boundaries between land and water surfaces in the data. There appears to be no significant shift overall across many different observed boundary orientations, including for example on circular features. The results from the thresholding method appear to be significantly more accurate than the manually mapped ones. This expected in terms of the more accurate georeferencing used later, as the average difference between the estimated shoreline positions is now only ≈4m – see Figure 23.

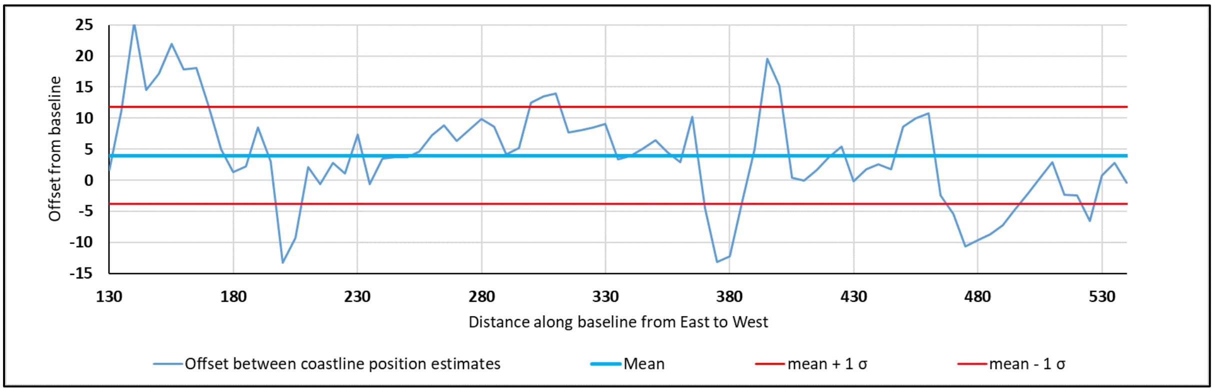

Figure 23 Distance or offset normal to the baseline between the coastline manually mapped at the cliff-top edge or the vegetation line in places with no edge. The mean offset [blue horizontal line] and 1 standard deviation around it [red horizontal lines] are superimposed over it to assess the general fit and quality of the data in aggregate.

As can be seen from Figure 24, there is significant variance in the offset, which is from the thresholding result. This suggest that the results are comparable to within the ≈5m spatial resolution of the Backscatter data. These differences are due to the larger variance in the Backscatter data as an effect of speckle noise, which is still present in the image (see e.g., Figure 24).

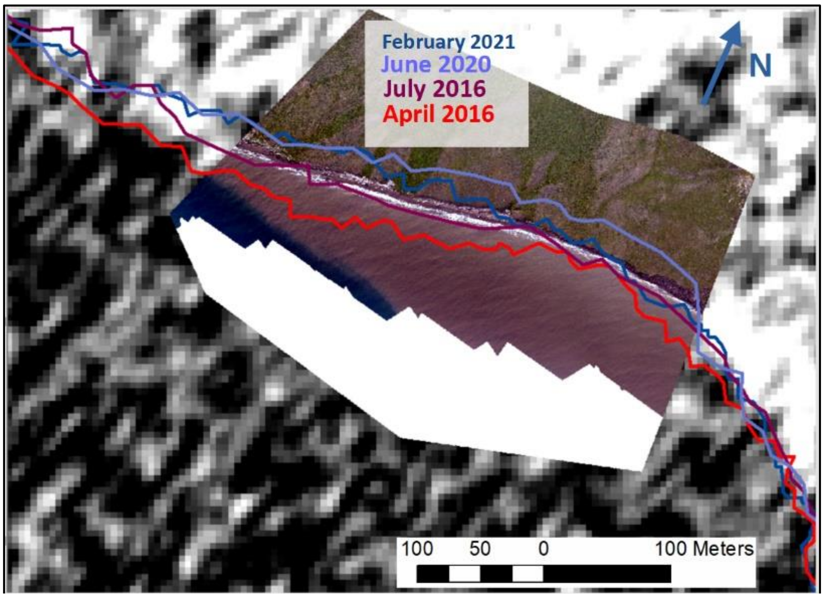

Figure 24 The manually mapped coastline from 4 points in time are displayed as in Figure 22. The drone photography is shown in colour over the SAR scene from April 2016 in black and white in the in dB background.

5.5 Coastline positions from Coherence thresholding

The stacking of Coherence data proved very successful in improving the image quality: With the visual difference between a single Coherence estimate between two scenes barely showing Herschel Island due to the high noise level and a stack of Coherence estimates clearly showing the islands outline and features, compare upper and lower image in Figure 25. The stacked data largely resembles the Backscatter data of individual scenes such as in Figure 21.

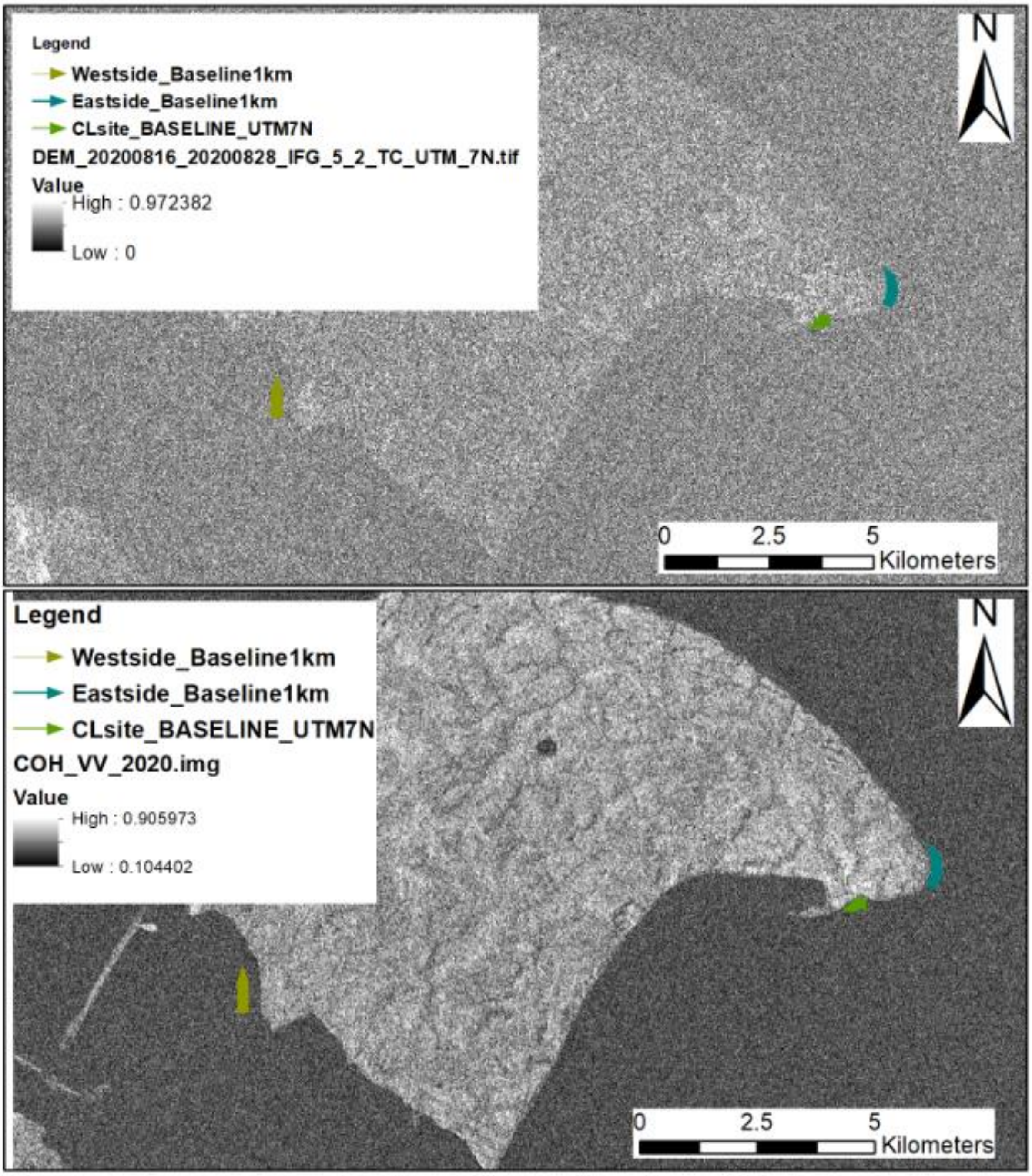

Figure 25 Coherence estimates for Backscatter data with Vertical-Vertical (VV) polarisation acquired on ascending orbits from summer 2020. The upper figure shows a Coherence estimate between two SLC scenes, where Herschel Island and its boundaries are not clearly visible. The lower figure represents the stacked and normalised (the averaged) Coherence estimate from 5 individual estimates based on 6 SAR scenes. The three site baselines are marked in lime, green and cyan showing orientation with arrow markers (not clearly visible at this scale).

The coastline positions have been mapped and displayed here for only Site 2 based on the Coherence for an ascending orbit, see Figure 27. This estimate is based on manual tracing of the increase in Coherence observed directly at the coastline. This increase is clearly visible in the stacked Coherence estimate from 2019, see Figure 33 showing a portion of Site 2.

This follows a zone of low Coherence directly before it, marked in Figure 33. The position estimates are grouped very closely together, when compared with Figure 17 and Figure 40. This leads to a very low erosion rate estimate of 1.62 m/yr. on average with also lower uncertainty or spread in the data, with the standard deviation being only ±1.8 m/yr. on average. The prediction for the 2025 coastline position based on a linear fit of the data also show little movement, with the observed and two predicted positions being almost exclusively within the margin of error of each other. The margin of error around the erosion rate is large enough that a positive erosion rate cannot be assumed with 90% confidence. Multiple outliers in the data and the outliers in the prediction have been removed. Moreover, not all positions have been detected with thresholding each year, such that the several predictions are missing or removed, as they are the result of obvious misclassification. These would plot outside the plot range and have little value towards estimating coastline positions.

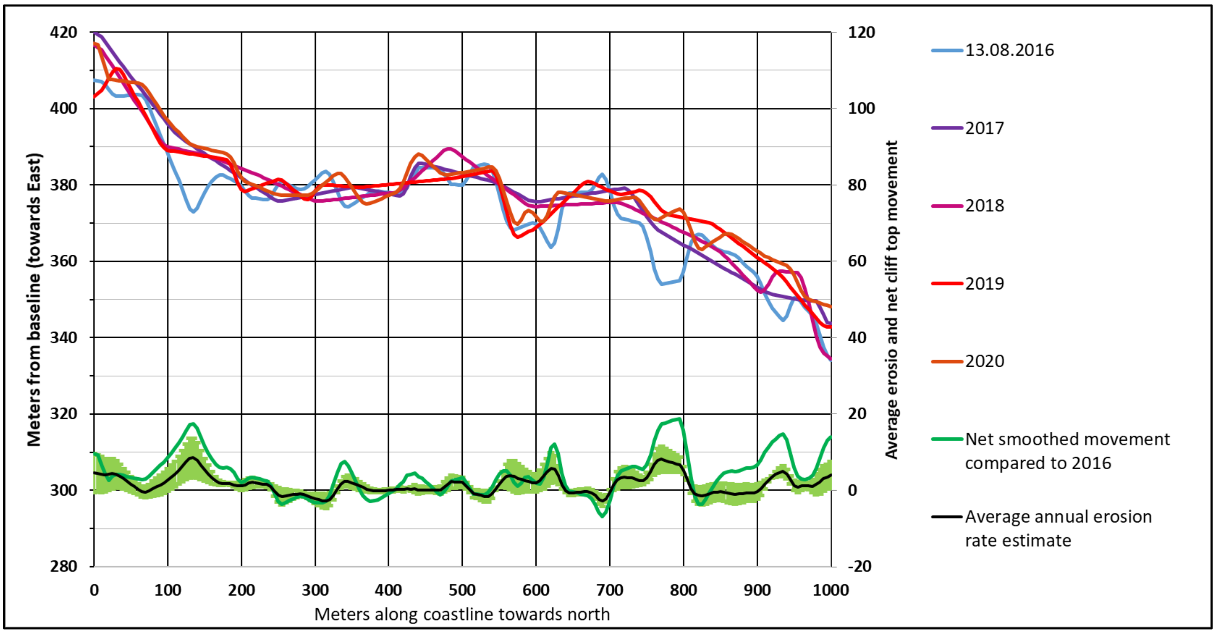

Figure 26 Coastline position estimates at Site 2. For each year the manually digitized positions based on stacked Coherence estimate from 2017 to 2020 and a single Coherence estimate from 2016 as blue to orange lines, left vertical axis. On the right axis (same scale but with an offset of 300 m) the net difference between the earliest and last position estimates (2016 and 2020) has been marked with the dark green line. Also on the right axis is the black line representing the average yearly erosion rate with the standard deviation of erosion rate estimates (green error bars) based on comparing each year with the 2016 dataset. Positive values represent erosion, negative values represent coastline progradation seawards by accumulation of sediments. The data was observed on an ascending orbit with looking direction towards East, positive y axis direction. The point spacing along the baseline is 5m, with 201 values plotted on each line.

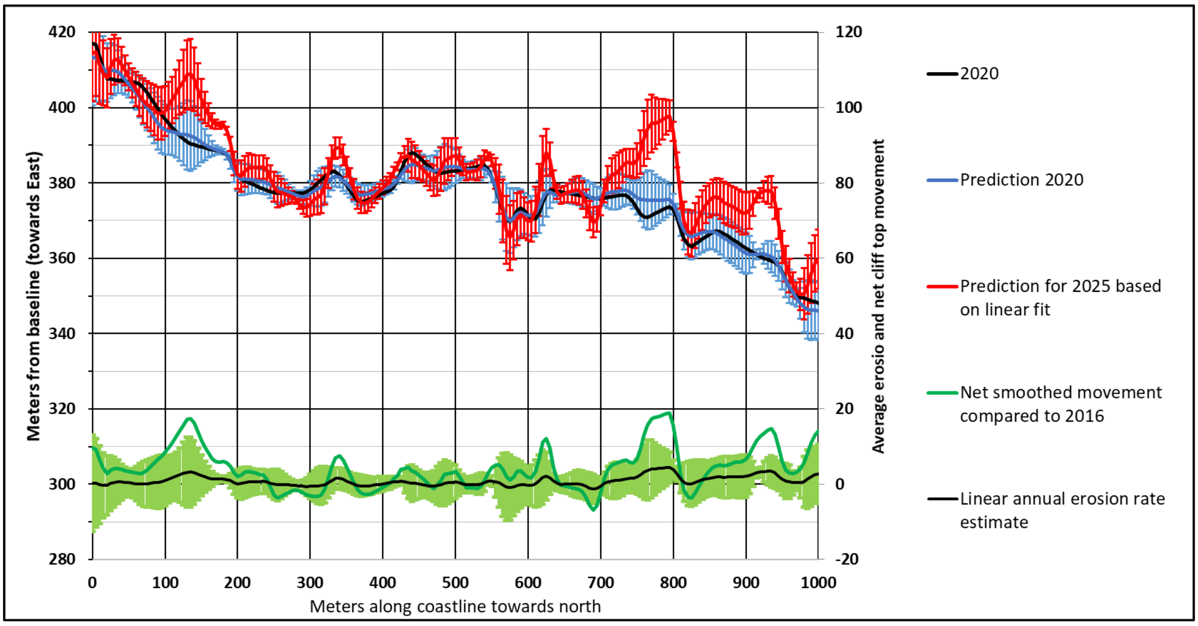

Figure 27 Coastline position estimates at Site 2. The observed 2020 position estimate (upper black line, left axis) is displayed with the estimated 2020 position from a linear fit at each point along the baseline. This estimate is based on the data displayed in Figure 26. On the right axis (same scale but with an offset of 300 m) the net difference between the earliest and last position estimates (2016 and 2020) has been marked with the dark green line. Also on the right axis is the black line (around the zero position) representing the yearly erosion rate based on the linear fit with the margin of error of the yearly erosion rate (green error bars) representing the 90% confidence interval at each point along the baseline. The data was observed on an ascending orbit with looking direction towards East, positive y axis direction. The point spacing along the baseline is 5m, with 201 values plotted on each line.

6 Discussion

6.1 General conditions

In terms of general conditions for SAR imaging, the data quality is expected to be very high. There are virtually no spatial ambiguity effects resulting from the non-unique range resulting from step terrain geometry. This is very advantageous here as the incidence angle for the SAR signal pulses lies between 43 and 46°.

The original resolution of the SAR data with 13.86m in azimuthal direction (approximately North-South considering the orbital path) and 3.86m in range direction (East-West, normal to flight path). Using simple trigonometry assuming that the radar pulse front is approximately flat at the observation scale, the horizontal ground range resolution (approximately E-W direction in the SAR scenes) is estimated at 5.22m. Relative to this, additional uncertainty is introduced in the detected coastline from the threshold value due to the tides and wave action. These coastal factors, although typically of small vertical variation may change considerably the horizontal position of the waterline and therefor the border of high Backscatter depending on how flat the beach is at the study site viewed here. Due to the lack of precise information about this additional uncertainty, the resolution and corresponding uncertainty of the coastline position are estimated from the data itself. Particularly as the data is resampled in the Terrain correction process, which does not consider different resolution in azimuth and range directions. The coastline manually mapped for April 2016 has a difference in position of up to 40m to the accurately mapped coastline from the drone photography for July 2016, despite the time interval between these datasets being only 3 months. This difference is considered too large to be due to actual erosion, as even with a rate of up to 1.1

m/d., Cunliffe et al. (2019), this was only episodic and yearly erosion rate estimates are much lower than this would suggest. The SAR scenes as GeoTIFFs produced by SNAP are only georeferenced automatically to an accuracy of ≈20m to the precise position due to the inherently low resolution. The terrain correction based on an external DEM generated from an ALOS-PALSAR dataset should not add much positional uncertainty to this, as it is interpolated, which should be reliable considering the mostly flat topography. The positioning appears to be accurate to the pixel level, see Figure 28.

Areas of higher Backscatter around the coast, which may be image artefacts or sea-ice directly attached to the coast may also give the impression of the coastline lying further seawards than it is. The speckle filter applied worsens this effect as it removes large variations at the individual pixel level. This may already result in individual pixels being misclassified when manually mapping the coastline considering the variations in the data in Figure 22 for example. When the data quality is exceedingly low, as in Figure 36 for example, mapping the coastline in this way is not feasible. The interpretation made here regarding the large position difference between the coastline estimates from the method used here and from Cunliffe et al. (2019) is as follows: there is randomly higher Backscatter directly at the coastline through the insufficiently filtered speckle effect or patches of coastal ice. Further factors which may contribute to this are the inaccurate georeferencing.

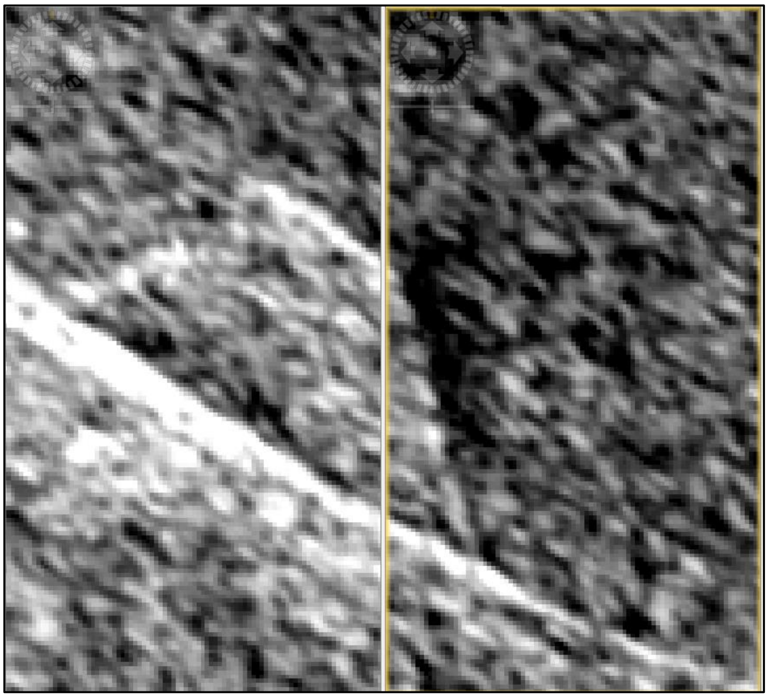

Figure 28 Alignment of two small parts of two SAR scenes with same zoom level within SNAP, showing two scenes divided by the yellow line in the middle are aligned to within pixel level of 5.68m. The feature shows how well the scenes are georeferenced with no clear gaps or offsets up to the pixel level.

6.2 Ascending vs. descending orbit: Comparing results from coastline orientations towards, away and parallel to sensor direction

A key question here is if the results are comparable considering the sensor orientation, comparing orientation away from the coastal slope or cliff surface and facing towards this surface.

The effect of sensor direction relative to coastline orientation appears to be quite large on the success of accurate mapping. Sensor direction is ≈88.15° on an Ascending orbit, facing close to exactly East and is then facing 180° from this towards West on a descending orbit. This has been an issue mentioned in Stettner et al. (2017), where the cliff area could only be fully observed when the sensor is facing in landwards direction towards the area.

The results from the sample sites 2 and 3 (West- and East-side sample areas) show a clear difference in data quality between acquisitions with the SAR sensor facing toward and away from the coastline. In both cases the results from data acquired with sensor facing towards the coastline shows much more potential for accurate and reliable erosion rate estimates. This is attributed to significantly less variance interpreted as misclassification, by a factor of 3 for Site 2 and a factor of over 10 for Site 3.

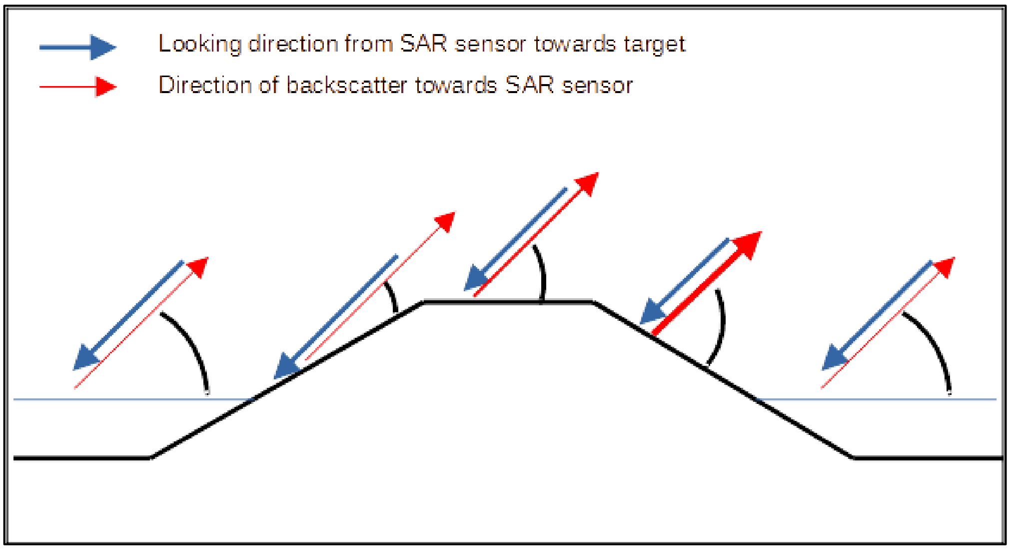

Figure 29 relative incidence angle based on looking direction. The black line represents a simplified cross-sectional sketch of the island's topography with same azimuth as the sensor looking direction shown here from the right. The blue arrows show the ≈45°. The actual local incidence angle on the horizontal close to planar surface of the island, varying between 42° further away from sensor and 46° closer to sensor on the island. The Backscatter intensity is also a function of the incidence angle, which changes depending on the topography and surface morphology of the target and the direction of slope. The relative Backscatter intensity is marked with the thickness of the red arrows. This relationship with the incidence angle is based on the figure from Mouginis-Mark (1996), see Figure 35.

The variance for these results being much lower when the sensor is facing towards the coastline is likely an effect of the steeper topography directly at the coastlines. The main reason for this is interpreted as the change of local incidence angle as displayed in Figure 29. On the coastlines facing away from the sensor, the relative Backscatter intensity is lower on all areas sloping downwards in the looking direction. The inclination of the slope at Site 2 is estimated as 5-21° and at 14-23° at Site 3. This leads to many pixels at and around the coastline being classified as water are due to lower Backscatter. The more inclined slope at Site 3 on the Eastern side of Herschel Island compared to the western side at most of Site 2 is then assumed to cause the larger variance at Site 3 compared to Site 2 in results with looking direction seawards at each site, see Figure 40 and Figure 42. Assuming Figure 35 shows linear scaling of normalised intensity compared to incidence angle, this results in a Backscatter intensity which is 3.6 dB lower on the slope at Site 3 than on most of the surface of Herschel Island which is near horizontal. This lower intensity is misclassified as water surface as it is no longer separated from the distribution of intensity observed for the water surface, see Figure 30, where there is already no complete separation in the distribution. This interpretation is favoured over the idea that range ambiguities depending on slope orientation are responsible for the variance on results for two reasons. The first being that lower Backscatter intensity is observed further than

200m landwards from the coast in place. This is over an order of magnitude more than would be reasonable if resulting from the range ambiguity effect, as the steep cliff-side directly at the coast is maximally 10m high. Considering the incidence angle of around 45°, the range ambiguity should not be of a larger order of magnitude than this height. The second reason is that assuming the cause is the range ambiguity, much less variance in the Backscatter than observed would be expected in the position normal to the looking direction.

6.3 Effect of season and sea-ice cover

In addition to the change in Backscatter characteristics caused by the variable sea and ground ice & snow cover, the level of speckle noise present in the scene appears to be affected as well. As the data has been filtered, see speckle filter step in Chapter 4 and Figure 5, this effect should not prevent accurate mapping. This effect should still be considered as it may introduce noise in the line objects representing the coastline at the pixel scale. In Figure 21 the speckle effect appears to be much greater during the winter season with high level of snow and ice coverage. To assess the speckle effect or noise in Backscatter intensity, the noise level is compared over a sample area on land and one over water. These two small areas are chosen to represent only data from land or the water and thereby can be assumed to have nearly uniform Backscatter intensity without considering the speckle effect. The variance in the sample area is then assumed to approximately represent the noise introduced by the speckle effect. The results are listed in Table 2 and show that the variance over both water and land areas is comparable between data acquired in summer and winter. There is a significant difference when comparing the mean of the land and water sample areas between summer and winter acquisitions. The thresholding method depends on the Backscatter distributions of land and water surfaces being separated. This separation must be near complete to avoid large variations in the boundary or coastline positions estimates, which is not the case in the data from the winter season. The difference mean between the land and water sample areas for VV polarisation is 7.6 dB in the summer but only 3.04 dB in winter. This the main factor which prevents an accurate delineation of the coastline as too much variance is introduced to the shoreline position to obtain useful results in most cases for the data acquired in winter.

In Figure 30 the Backscatter intensity distributions are given for a scene as an example for winter and summer season for both polarisations. There appears to be no significant difference between Backscatter distribution based on polarisation and directional dependency of the land and water surface reflectivity. A large difference between the winter and summer Backscatter values is clear from Figure 30: While the data acquired during summer shows a bimodal distribution, the data acquired during winter shows single maximum. The second, smaller peak in the summer data, see right side of Figure 30, is interpreted as the Backscatter distribution over land, which is significantly higher during the summer as is clear from Table 2. The Backscatter intensity distribution for the water surface is represented in the larger peak of lower intensity which matches the overall larger proportion of water surface in the SAR scenes. The threshold by which pixels are classified as land or water is marked with black vertical lines in Figure 30. It is positioned in the local minimum in the summer data and on the right-hand slope of the peak in the winter data, displaying very clearly that the land and water Backscatter value distributions are only effectively separated for the summer season. The ground freezing and snow cover in the winter is assumed to cause the Backscatter intensity to be reduced for the land surface; more strongly when the surface layer begins to melt or become wet, see Buchelt et al. (2021).

Mapping the coastline during the winter season therefor is difficult. It is further complicated by thin ice directly at the coastline having different Backscatter response than far from land, see Tan et al. (2018).

Table 2 Backscatter variations on land and water depending on season and Polarisation. The sample area locations for which the following statistical values are listed are marked in Figure 34.

		Backscatter mean and variance	
Sample area	Polarisation, VV = Vertical-Vertical, VH = Vertical-Horizontal	With high ice cover – "Winter" April 2016	With low ice cover – "Summer" July 2016
A: Land	VV	-25.15 ± 5.39	-20.31 ± 5.02
	VH	-16.97 ± 5.83	-13.40 ± 6.43
B: Water	VV	-28.19 ± 4.19	-27.91 ± 4.22
	VH	-23.76 ± 3.75	-22.13 ± 4.29

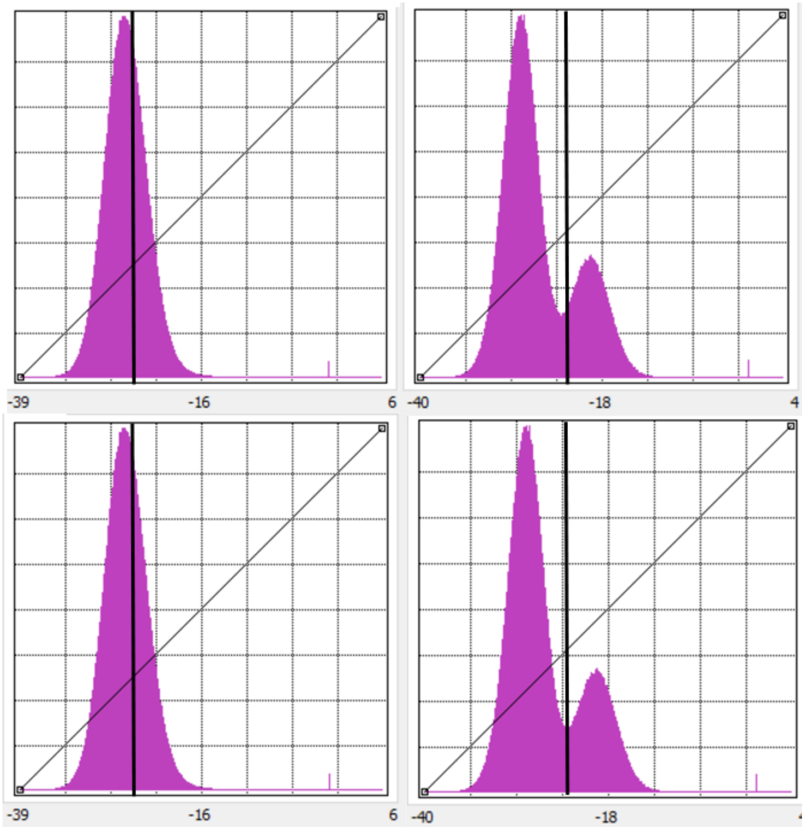

Figure 30 Backscatter intensity histograms for an entire scene observed on ascending orbit from the summer and winter season as an example. The vertical axis is not given as this is only a preview figure and shows pixel counts which are not used further. The maximum on the vertical axis value is ≈35000, the horizontal axis values are given in decibels (dB). Left: Backscatter distribution from VV polarisation (top) and from VH polarisation (bottom), observed 15.04.2016 -Winter season. Right: Backscatter distribution from VV polarisation (top) and from VH polarisation (bottom), observed 08.07.02016 – Summer season. The black vertical line represents the threshold value chosen for the Winter and Summer season – the threshold is the same for all polarisations.

6.4 Comparability to other means of obtaining coastline data: Comparison with drone imagery from Cunliffe et al. 2019 and other previous studies

As the composite drone images from Cunliffe et al. (2019) from two years are available as precisely (sub-0.5m accuracy) georeferenced GeoTIFF files, it presents the data and results from a previous study which are highly accurate and most directly comparable with the Sentinel-1 SAR-based study here. It then raises the question of whether the SAR-based results are validated by the drone imagery and what the key differences to be considered are when making a comparison. In light of the effect of sensor orientation, it should be noted that the interpretation of this subchapter is made only for data acquired with the sensor not facing away from the coastline (i.e. line of sight [LOS] intersects with the coastline from the sea direction).

The main results mapped from the Backscatter data for July 2016 do lie further seawards than the cliff-top seen in the drone imagery, seen when comparing the offset or distance to the positions from the drone imagery both the manually mapped coastline in Figure 23 and the coastline mapped with thresholding in Figure 31 showing similar patterns. This is interpreted as the beach up to the water line showing higher Backscatter and thus being classified as land surface. This matches the expected variation in the line, with the positions from Backscatter data forming a much less straight line overall than the visible cliff top. This is interpreted as being caused by wave action (see white fringe in drone-based image in Figure 24) with the waterline being closer or further away from the cliff-top at various points. This has a similar effect to the inherent speckle noise in the SAR image, but this combined effect does not appear to add significant additional variance in the difference between the results from the two methods.

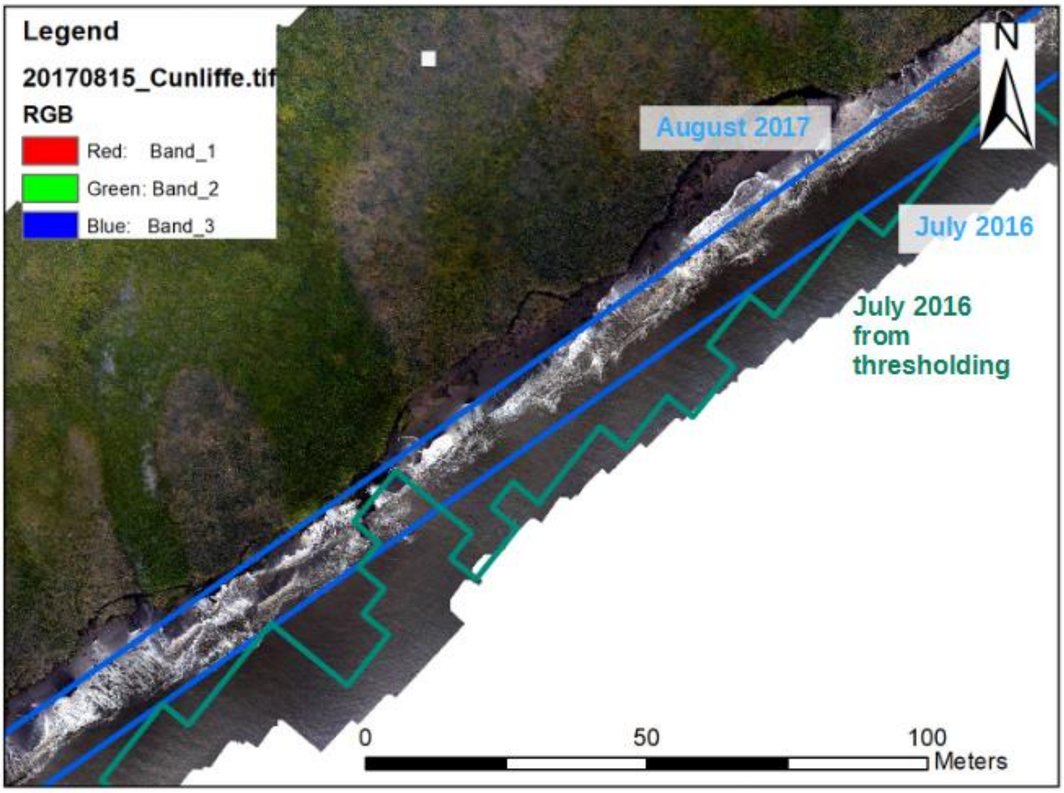

Figure 31 Composite drone imagery modified from Cunliffe et al. (2019) acquired 15th August 2017 at the middle area of Site 1. The blue lines mark the approximate positions of the cliff-top not considering areas eroded further, i.e., through block collapse for this background image (upper blue line) and an image from July 2016 (lower blue line). The distance between these blue lines is 11-13m. The teal line with the pixel pattern shows the coastline estimate from thresholding for the July 2016 ascending (looking East) Backscatter data.

This variance effect could be manually corrected for or filtered out if the maximum realistic coastline roughness can be considered. Particularly spikes of higher difference and positions in the SAR results further seawards could be corrected towards surrounding values. The positions in the SAR lines lying significantly further landwards than their surroundings are interpreted as being caused by lower Backscatter from certain areas directly below the cliff-top line. These are the areas below the cliff covered in broken off parts of the cliff and partially wave-smoothed smoothed debris that are visibly eroded further than the value 2017-line marker in Figure 31. These structures have increased random omnidirectional scattering of the incident signal and are then classified as water pixels as the Backscatter intensity recorded is then lower than the thresholds applied.

The results from the thresholding with spikes of higher variance are then not representing accurately the actual morphology of the coast on a small scale, but overall do determine the coastline position reliably, albeit with low precision. This variance is expected to be larger for the low-lying coasts with short cliff of few meters height, as is the case at Site 1, with the area around this site being largely less than 10m above sea level. As there are many crossings of the mean value in the offset, the aggregated results are assumed to represent the coastline position very reliably relative to the positions from other times generated also using the Backscatter thresholding method. The mean offset of ≈5m between the results from these two different methods, see Figure 23 should not be used as an indication the Backscatter results are less comparable with each other by this value, as this is around the level of uncertainty inherent in the Backscatter data given with 5.9m pixel spacing.

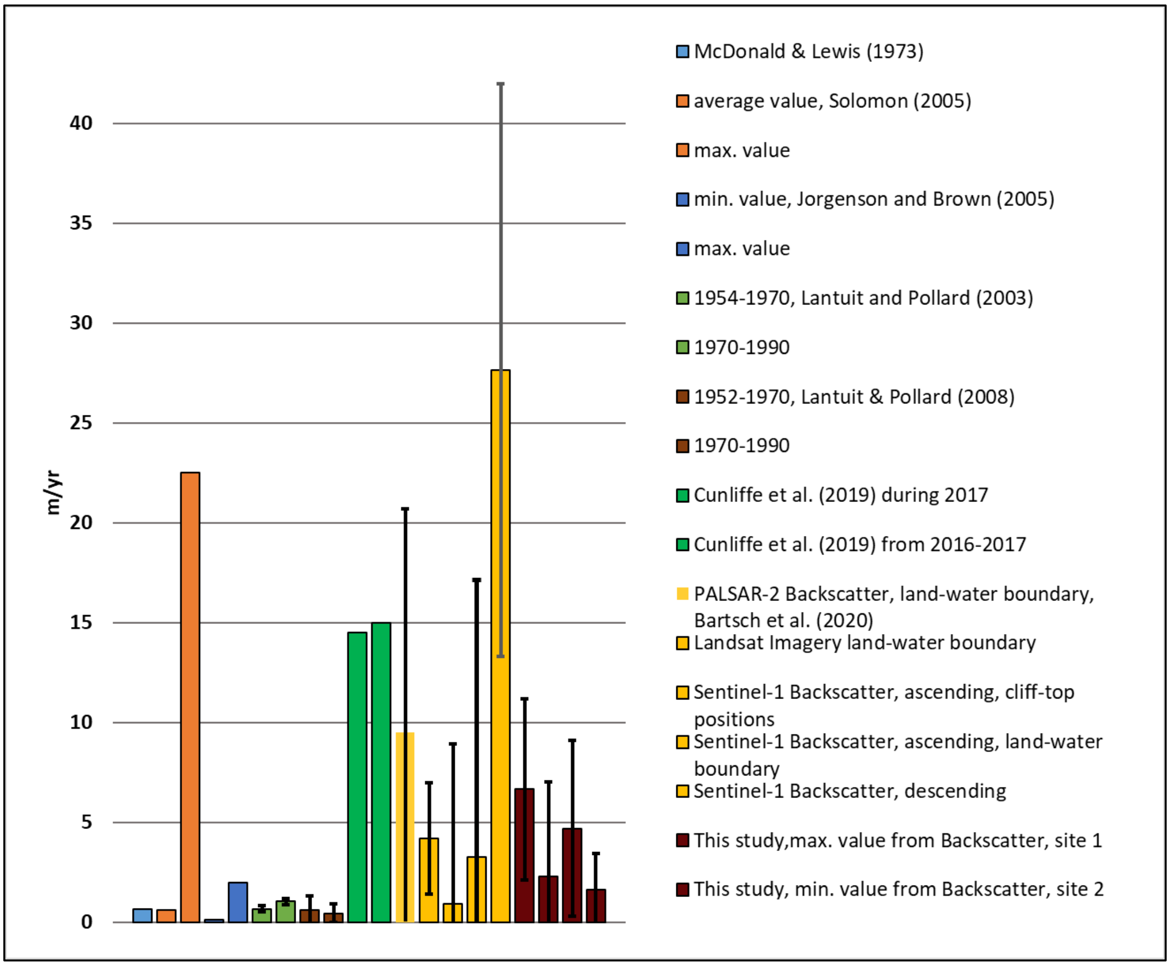

Figure 32 Column chart of results from multiple previous studies and this one as listed in Table 3, with the individual results from this study marked, while only the average is given in the table. Minimum and maximum values are given as separate columns; the level of accuracy or uncertainty is displayed if given for the data as a black vertical error bar.

Table 3 Comparison of results for coastal retreat rates on Herschel Island and other permafrost coast in the Beaufort Sea region. Only positive rates are considered, although negative erosion rates signifying accretion have been mentioned in several studies and possibly observed in the results for this study.

Source	**Data, Method used**	**Time frame**	**Location(s) & comments**	**Average result**
McDonald and Lewis (1973)	Uncorrected Aerial photos	1944-1970	Entire coastline of Herschel Isl.	0.66 m/yr.
Solomon (2005)	Aerial photos	1972, 1985, 2000	Coastlines in the southern Beaufort Sea	0.6 m/yr., max. 22.5 m/yr.
Jorgenson and Brown (2005)	Orthorectified Aerial photos	1955, 1979, 2002	60km segment of the Alaskan Beaufort Coast	0-2 m/yr. for most locations
Lantuit and Pollard (2003)	Orthorectified high-resolution aerial photo digitization	1954-1970	Entire coastline of Herschel Isl. Except westmost part of Isl.	0.67 m/yr.
		1970-1990		1.03 m/yr.
Lantuit and Pollard (2008)	Orthorectified high-resolution aerial photo digitization	1952-1970	Entire coastline of Herschel Isl. Except westmost part of Isl.; Mean and STDEV of shoreline retreat rates with accuracy	0.61 ± 0.71 m/yr., accurate to ±0.14 m/yr. -
		1970-1990		0.45 ± 0.48 m/yr., accurate to ±0.07 m/yr.
Lantuit and Pollard (2012)	Remote sensing imagery, from sources above and multiple other sources	1950 - 2010	Hershel Island specifically from all available data	0.5 - 1.2 m/yr.
Cunliffe et al. (2019)	Drone Imagery	2017: observations during 40 days	Site 1 on south-eastern facing shore, see Figure 4	14.5 m/40 d
	Comparing Drone Imagery visually	2016 and 2017	Site 1 on south-eastern facing shore of Herschel Island, see Figure 4	15 m/yr
Bartsch et al. (2020)	PALSAR-2 Backscatter, land-water boundary	2017-2018	Avadlek, north-western facing shore on Herschel Island	9.52 ± 11.2
	Landsat Imagery land-water boundary	1999-2014		4.19 ± 2.8
	Sentinel-1 Backscatter, ascending, cliff-top positions	2017-2018		0.9 ± 8.01
	Sentinel-1 Backscatter, ascending, land-water boundary	2017-2018		3.26 ± 13.88
	Sentinel-1 Backscatter, descending	2017-2018		27.63 ± 14.34
This study	Sentinel-1 SAR Backscatter land-water threshold	2016 to 2020	3 sites on Herschel Island, see Figure 4	4.7 ± 4.4 m/yr.

The erosion rate estimates based on the two methods are quite similar, with 7 m/yr. average estimate from thresholding but with values over 10 m/yr. ± ≈4 m/yr. along the majority of the profile and 13 m/yr. average estimated from the two drone images, see blue lines Figure 31 with 14.5m erosion for 2017 reported by Cunliffe et al. (2019). These results are of similar size, but importantly the results from Cunliffe et al. (2019) are episodic; while the results from thresholding indicate a similar medium to high average erosion rate that is less variable over time. Each observation of this study shows that coastline position is overall moving decidedly further landward each year.

Various other studies have been carried out to estimate coastal erosion rates, some of which have been introduced in Chapter 2. Table 3 lists the aggregated results compared with this study based on the previous studies of coastal erosion in the Hershel Island region. Figure 32 shows the results to quickly compare them visually. Overall, the results from the Backscatter thresholding appear to have a magnitude between the results estimated from aerial photography and those estimated from drone imagery. They are most similar to the results of Bartsch et al. (2020), which may be expected as one of the same data sources is used. It is not completely conclusive, as several of the results from this study show high margin of error. This is not unexpected given the lower spatial resolution of the input data.

6.5 Discussion of the thresholding method applied to Coherence data

The thresholding method was applied to the stacked Coherence estimates at Site 1 and Site 2, see Figure 37 and Figure 38, but not at Site 3. This is because at time of writing only Coherence estimates from SAR scenes acquired on an ascending orbit have been processed due to the higher processing time for the Coherence estimates. The stacked Coherence estimates from an ascending orbit show similarly low values, much like the Backscatter around the areas with a slope facing away from the SAR sensor. This has been an issue even for Site 1, see Figure 37, showing too high variance in the position to yield useful estimates of coastline positions for each summer, the coastline being aligned close to parallel to the sensor looking direction.

The coastline positions have been estimated more reliably based on manual digitization of the stacked Coherence estimates for each year, see Figure 26 compared with the results from thresholding showing much more variance, see Figure 38. For the thresholding result, many pixel clusters were misclassified, and the resulting morphology based on the estimates is much too complex to be considered realistic, with variations of up to 80m along short distance along the coast. The yearly position estimates based on manual digitization of the coastline from the stacked Coherence shows significantly less variation than the position for each year based on Backscatter thresholding. This is due to the Coherence estimation having low values in zones of rapid change such as the beach with water line changing quickly with each wave, seeFigure 33. This low Coherence reduces the change in results from smoothing effect on the seaward side inherent in the data from the 5×2-pixel window (range and azimuth size) used for the Coherence estimation. The Coherence estimates act as a filter, removing effects which change the Backscatter properties faster than the 12-day repeat pass frequency. This leaves the zone directly above the waves, which shows high Coherence as it changes much more slowly, with a time interval of over 2 months between scenes showing decorrelation here too. In this way the Coherence estimates likely image the top of the slope directly above the water, which provides an accurate way to measure erosion based on the actual topography. If the elevation is known precisely, this could also allow volumetric erosion rate estimates. The linear or planimetric erosion rate is expected to be estimated more accurately than the given E-W spatial resolution of the raw Backscatter data of ≈5.2m would imply. This is due to the data being resampled to a smaller pixel size of 3.8m and 5-6 SAR scenes being used to generate the coastline position for each year. Using this many datasets in total averages out the estimate and is assumed to improve at least the erosion rate estimate, if not the absolute position estimate. This is expected to be true even if there is a systematic bias in the absolute position of the coastline for each Coherence estimate such as from inaccurate Terrain Correction. This is due to the assumption that a given bias is not expected to change a significant amount between each year as the imaging geometry (e.g., incidence angle) does not change significantly and the actual erosion rate is assumed to be low. In simple terms, the error in erosion rate should be always lower than the total position error, as over 20 SAR scenes are used in total to generate the data in Figure 26 and Figure 38.

The lower Coherence values on slopes facing away from the sensor looking direction is assumed to be possibly caused by inaccurate conversion from slant range to ground range geometry, especially if the DEM or DSM used is not highly accurate or well-interpolated if in low resolution. This is based on the distortions in the data observed on many sloping surfaces facing North, East and South, with different effects observed depending on direction. Another factor reducing Coherence is the changing ground Backscatter properties due to small differences in e.g., temperature or ground wetness. That the Coherence is not completely uniform on the largely flat area not directly at the coast can be seen in Figure 25 despite the relatively poor image quality here.

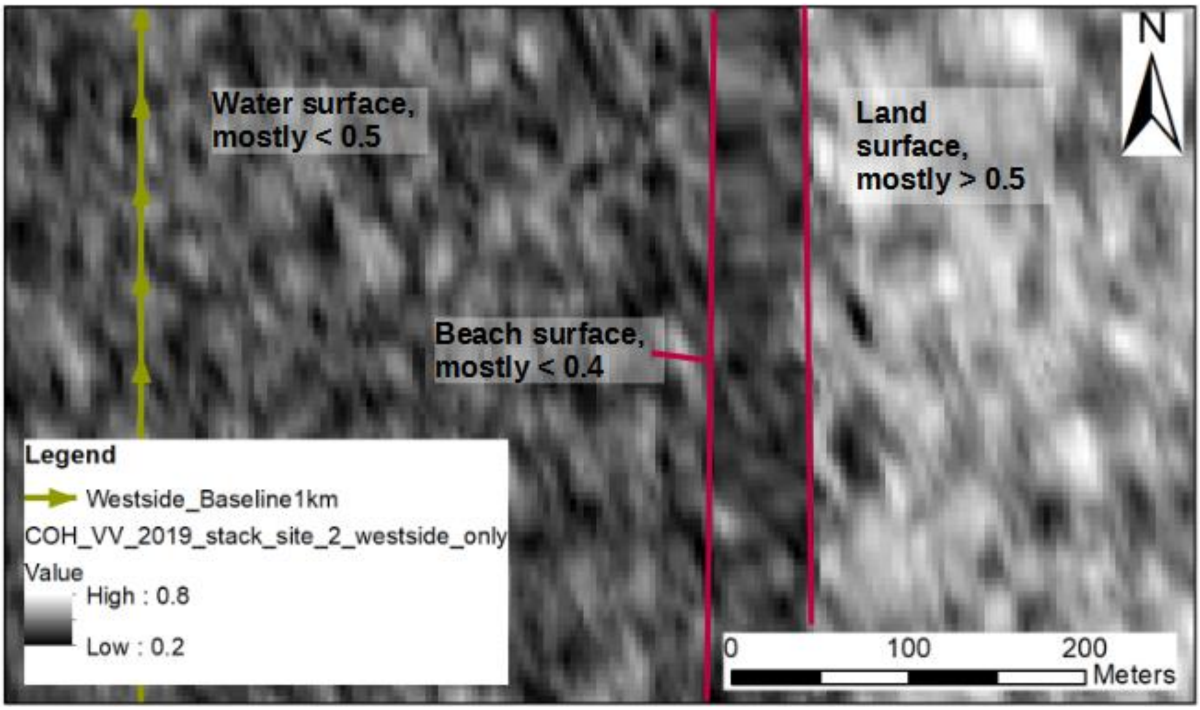

Figure 33 Stacked Coherence from 5 Coherence estimates between each pair of datasets in chronological order for summer 2019, based on Backscatter data with VV polarisation acquired on an ascending orbit, showing a small part of Site 2 in greyscale. This area is selected to illustrate the three zones showing different Coherence distributions. From left to right: Sea surface showing high levels of random noise with Coherence values from 0 to 0.5; the beach or wave zone marked with magenta lines showing very low (<0.4) Coherence; the land surface on the right showing very high Coherence values between≈ 0.5 and ≈0.95.

7 Conclusions

7.1 Usage of Backscatter data for monitoring ACR

Generally, the mapping of coastline positions on a yearly basis with SAR data acquired with Sentinel-1A based on Backscatter intensity thresholding has been successful. This is based on the erosion rate estimate being higher than the 90% confidence interval, especially for the sample Site 1: Cunliffe site. This did not succeed as well for sites 2 and 3, which is a here largely attributed to the lower average erosion rates observed at sites 2 and 3. The results of this study indicate larger, on average 6.65 m/yr. erosion rates at the South-East facing shores (represented by Site 1) with lower 2.7 m/yr. rates observed in other areas, represented by study sites 2 and 3. These results are supported by the comparable erosion rate results from various other studies of coastal erosion rates on Herschel Island, as listed in Table 3. Much like the results from the other studies indicate, the majority of coastlines are eroded slowly with specific stretches having vastly higher rates.

7.1.1 Sensor direction on Ascending and descending orbit relative to coastline

Interpretation of the results requires strong consideration of sensor direction. The results from all three sample sites indicate that coastline positions are best estimated from areas facing the sensor. Poor results with high misclassification rate, margin of error and variance are otherwise obtained.

7.1.2 Seasonal differences and sea-ice cover effects

The seasonality observed over the course of each year in the SAR data strongly favours the use of data acquired during the summer season, which supports the conclusions from Bartsch et al. (2020) and Short et al. (2011). As can be seen from Figure 10 and Figure 21, the thresholding method can be expected to perform reliably when the other factors such as sensor direction are favourable. The thresholding method is still functional during the winter season but limited to ice-free intervals of coastline. The data quality was generally high during the summer season, with 1 of 10 datasets being of too poor quality for thresholding use. High levels of noise were often observed during the winter season, with the results of 7 from 14 datasets being unreliable here.

7.1.3 Weather conditions and data quality

The data quality is generally high, with only 1 dataset from all 24 used for Backscatter thresholding being completely unusable for this purpose due to noise or other image aberrations. The choice of data acquired in IW [Interferometric-Wide Swath] mode is practical, as a scan type called Terrain Observation with Progressive Scan (TOPS) is implemented, see website of the European Space agency on Sentinel-1 in the bibliography. Due to this mode of acquisition, a range of benefits for the SAR imaging process are achieved: Coverage and resolution remain high, with signal to noise ratio and target point signal spread from using a synthetic aperture being highly uniform across the entire SAR scenes.

7.2 Usage of Coherence data to monitor ACR

The thresholding method was applied less successfully to the Coherence data than to the Backscatter intensity data. The Coherence estimates from each year were successfully stacked for 2018 to 2020, enabling visual coastline position estimates by manual digitization. The thresholding results show a high margin of error, which makes the results unreliable, especially for the low observed erosion rate. The thresholding method requires further modification to be of use but based on the manually mapped results it shows to be actually more promising for accurate monitoring of coastal erosion. In particular, it appears to image the cliff-top or other area above the fast-changing wave zone rather than the first area with higher Backscatter. It should be notes that the Coherence estimate is only of good quality on coasts facing towards the sensor, limiting the application to specific orientations more strictly than is the case for Backscatter intensity thresholding.

8 Outlook

While the concept of using Sentinel-1A SAR Backscatter and Coherence data to monitor coastal erosion rates could be demonstrated here, the approach remains limited by factors such as seasonality, coastline orientation and noise inherent in the data. The application of this approach could benefit vastly from improvements in automatic classification and filtering at various steps in the processing. In particular, better speckle filters for the raw radar data, for example a SAF or an adaptive Frost filter, see Kupidura (2005), could give better input data for the thresholding. A morphological filter to remove outlying clusters of misclassified pixels, which form a contiguous area with the land surface in the image leading to high variance in coastline position estimate could improve the reliability and accuracy considerably. Pixels classified in patches along the coastline, as is the case for the Coherence thresholding results require manual connection of the line objects to cover the full stretch. An interpolation approach for these line objects based on vertex distance could make these result useable without manual additions to each result, greatly improving the speed at which results can be generated. More generally an automatic download and subsequent selection of scenes from the available data could save visual checking of data quality. This could be based on image quality and pixel clustering from the binary images generated with the thresholding. The lower quality data generally results in more separate clusters and much higher length of line objects generated overall, which could be used to sort out unreliable results automatically.

9 Bibliography

Software, data and Website References

ArcGIS

ESRI ArcGIS 10.8 desktop, advanced version, downloaded 2021, https://www.arcgis.com/index.html.

DSAS

Himmelstoss, E.A., Farris, A.S., Henderson, R.E., Kratzmann, M.G., Ergul, Ayhan, Zhang, Ouya, Zichichi, J.L., Thieler, E.R., 2018, Digital Shoreline Analysis System (version 5.0): U.S. Geological Survey software release, downloaded 2021, https://code.usgs.gov/cch/dsas.

SNAP

Sentinel Application Platform (SNAP) implementation for desktop 8.0.3, downloaded 2021, http://step.esa.int/main/toolboxes/snap/.

Source for confidence interval statistics

Online confidence interval calculator, https://stattrek.com/online-calculator/t-distribution.aspx, accessed 30.06.2021.

Sentinel-1 IW mode reference

European Space Agency website for technical details on the Sentinel-1 mission, accessed 02.08.2021, https://sentinels.copernicus.eu/web/sentinel/user-guides/sentinel-1-sar/acquisition-modes/interferometric-wide-swath.

Sentinel-1 data source

Alaska Satellite Facility, https://search.asf.alaska.edu/#/,

Orbit files in case of manual download

European Space Agency, http://step.esa.int/auxdata/orbits/Sentinel-1/, POEORB folder.

Literature References

Bartsch Annett, Ley Sarah, Nitze Ingmar, Pointner Georg, Vieira Gonçal, 2020, Feasibility Study for the Application of Synthetic Aperture Radar for Coastal Erosion Rate Quantification Across the Arctic, Frontiers in Environmental Science, volume 8, https://www.frontiersin.org/article/10.3389/fenvs.2020.0014, DOI: 10.3389/fenvs.2020.00143.

Bernhard Philipp, Zwieback Simon, Leinss Silvan, Hajnsek Irena, Mapping Retrogressive Thaw Slumps Using Single-Pass TanDEM-X Observations, IEEE Journal of Selected Topics in Applied Earth Observations and Remote Sensing, Vol. 13, 3263-3280, 2020, DOI: 10.1109/JSTARS.2020.3000648.

Bickel Doug, 2017, Coherence in Radar Processing for SPIE Radar Sensor Technology XXI, Conference: Proposed for presentation at the SPIE Radar Sensor Technology XXI held April 9-13 2017 in Anaheim, CA., Sandia National Laboratories, USDOE National Nuclear Security Administration (NNSA), 12 April 2017, accessed 01.08.2021, https://www.osti.gov/servlets/purl/1456496.

Buchelt Sebastian, Skov Kirstine, Ullmann Tobias, 2021, Sentinel-1 time series for mapping snow cover and timing of snowmelt in Arctic periglacial environments: Case study from the Zackenberg Valley, Greenland, the Cryosphere, https://doi.org/10.5194/tc-2021-78.

Cunliffe A. M., Tanski George, Radosavljevic Boris, 27 May 2019, Rapid retreat of permafrost coastline observed with aerial drone photogrammetry, The Cryosphere 13 1513–1528 2019, https://doi.org/10.5194/tc-13-1513-2019, Published by Copernicus Publications on behalf of the European Geosciences Union

Dallimore, S.R., Wolfe, S., Solomon, S.M., 1996. Influence of ground ice and permafrost on coastal evolution, Richards Island, Beaufort Sea Coast, NWT. Canadian Journal of Earth Sciences 33, 664–675.

Holsten, H., 2021, A literature review on application of synthetic aperture radar data to quantify arctic coastal retreat, unpublished literature review, RWTH University

Hoque Md. Azharul, Pollard Wayne H., 2016, Stability of permafrost dominated coastal cliffs in the Arctic, Polar Science, Volume 10, Issue 1, March 2016, Pages 79-88, ISSN 1873-9652, https://www.sciencedirect.com/science/article/pii/S1873965215300177, https://doi.org/10.1016/j.polar.2015.10.004.

Johnson, K., Solomon, S.M., Berry, D., Graham, P., 2003. Erosion progression and adaptation strategy in a northern coastal community. In: Phillips, M., Springman, S.M., Arenson, L.U. (Eds.), Final Proceedings, 8th International Conference on Permafrost, Zurich, Switzerland, July 20–25, 2003. International Permafrost Association, 8, pp. 489–494.

Jorgenson, M.T., Brown, J., 2005. Classification of the Alaskan Beaufort Sea Coast and estimation of carbon and sediment inputs from coastal erosion. Geo-Marine Letters 25 (2–3), 69–80.

Kupidura P., 2005, Comparison of Filters Dedicated to Speckle Suppression in SAR Images, The International Archives of the Photogrammetry, Remote Sensing and Spatial Information Sciences, Volume XLI-B7, 2016, XXIII ISPRS Congress, 12–19 July 2016, Prague, Czech Republic.

Lantuit, H., Pollard, W.H., 2003. Remotely sensed evidence of enhanced erosion during the twentieth century on Herschel Island,Yukon Territory. Berichte zur Polar- und Meeresforschung (Reports on Polar and Marine Research) 443, 54–59.

Lantuit, H., & Pollard, W. (2008). Fifty years of coastal erosion and retrogressive thaw slump activity on Herschel Island, southern Beaufort Sea, Yukon Territory, Canada. Geomorphology, 95, 84–102.

Lantuit, H., Overduin, P. P., Couture, N., Wetterich, S., Aré, F., Atkinson, D., et al. (2012). The Arctic Coastal Dynamics Database: A New Classification Schemeand Statistics on Arctic Permafrost Coastlines. Estuar. Coasts 35, 383–400, doi: 10.1007/s12237-010-9362-6.

Mackay J. R. (1959). Glacier ice-thrust features of the Yukon coast. Geographical Bulletin, 13, 5–21.

Mouginis-Mark P., 1996, Introduction to Radar Remote Sensing (Page 2): Radar Backscatter as a Function of Incidence Angle, Virtually Hawaii, an internet project funded by NASAS, http://satftp.soest.hawaii.edu/space/hawaii/vfts/kilauea/radar_ex/page2.html.

Short Naomi, Brisco Brian, Couture Nicole, Pollard Wayne, Murnaghan Kevin, Budkewitsch Paul, 15th September 2011, A comparison of TerraSAR-X, RADARSAT-2 and ALOS-PALSAR interferometry for monitoring permafrost environments, case study from Herschel Island, Canada, Remote Sensing of Environment 115 (2011) 3491–3506.

Ogorodov, S.A., 2005, Human impacts on coastal stability in the Pechora Sea, Geo-Marine Letters (Online edition), doi:10.1007/s00367-004-0200-3.

Smith, S., Burgess, M.M., 2000. Ground temperature database for northern Canada. Geological Survey of Canada Open File Report, vol. 3954. 57 pp..

Smith, C. A. S., Kennedy, C. E., Hargrave, A. E., & McKenna, K. M. (1989). Soil and vegetation of Herschel Island, Yukon Territory. Yukon Soil Survey Report, Vol. 1, Ottawa: Land Resource Research Centre, Agriculture Canada.

Solomon, S.M., 2002. Tuktoyaktuk Erosion Risk Assessment Report. Geological Survey of Canada, Natural Resources, Canada.

Solomon, S.M., 2005. Spatial and temporal variability of shoreline change in the Beaufort–Mackenzie region, northwest territories, Canada. Geo-Marine Letters 25 (2–3), 127–137.

Tadono, T., Ishida, H., Oda, F., Naito, S., Minakawa, K., & Iwamoto, H. (2014). Precise global DEM generation by ALOS PRISM. ISPRS Annals of the Photogrammetry, Remote Sensing and Spatial Information Sciences, 2(4), 71.

Tan, Weikai & Li, Jonathan & xu, Linlin & Chapman, Michael. (2018). Semiautomated Segmentation of Sentinel-1 SAR Imagery for Mapping Sea Ice in Labrador Coast. IEEE Journal of Selected Topics in Applied Earth Observations and Remote Sensing. PP. 1-14. 10.1109/JSTARS.2018.2806640.

Yonezawa, C., & Takeuchi, S. (2000). Land subsidence detection using long interval ERS/SAR data pairs. Proceedings of IGARSS 2000, 24–28 July, Honolulu, Hawaii. New York, NY: IEEE.

Yukon Government, Herschel Island - Qikiqtaruk Territorial Park, https://yukon.ca/en/herschel-island-qikiqtaruk-territorial-park, accessed 23.06.2021 © Copyright 2021 Government of Yukon.

Bush, E. and Flato, G. (2019): Chapter 1 in Canada’s Changing Climate Report, (ed.) E. Bush and D.S. Lemmen; Government of Canada, Ottawa, Ontario, p. 7–23ISBN: 978-0-660-30222-5, Canada's Changing Climate Report, https://changingclimate.ca/site/assets/uploads/sites/2/2020/06/CCCR_FULLREPORT-EN-FINAL.pdf.

10 Appendix

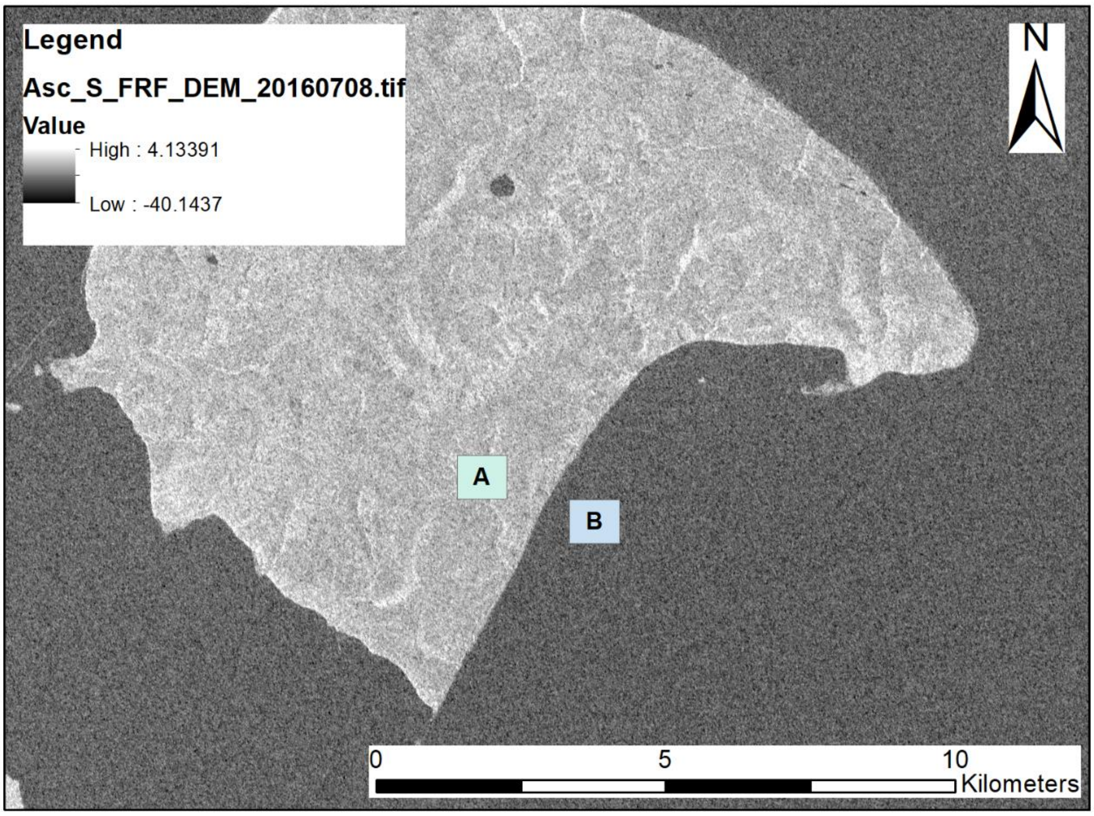

Figure 34 SAR scene based on ascending orbit from July 2016 in grayscale in the background with values in dB.. The areas marked A and B are the land and water sample areas used to evaluate the mean and variance. These two areas are arbitrarily selected to be of ≈1km² size and close to each other while it being certain that they are fully located on land or water respectively.

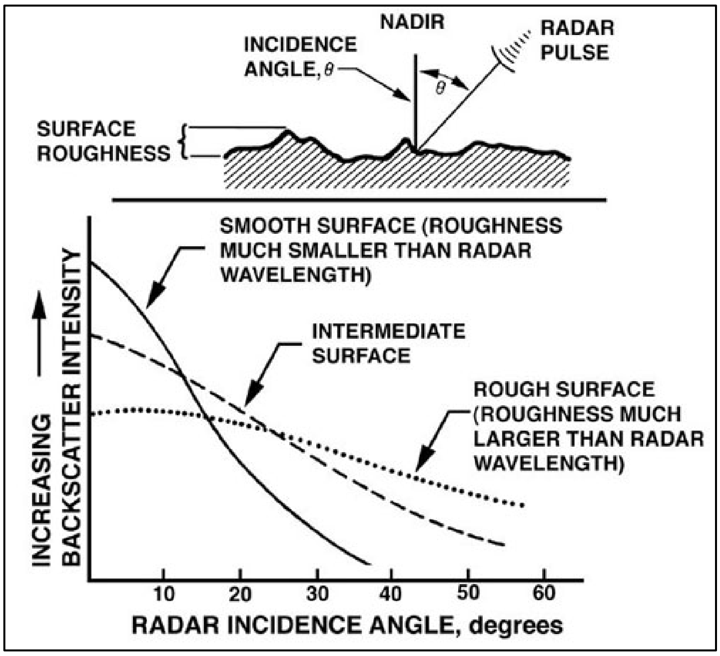

Figure 35 Angle dependent scaling relationship between backscatter intensity and incidence angle depending on qualitative size comparison of roughness (surface height variation) to Radar wavelength. The smooth topography of Herschel Island, with low-growing vegetation on the surface would represent an intermediate surface, with the wavelength of similar size to surface roughness. Source: Mouginis-Mark (1996).

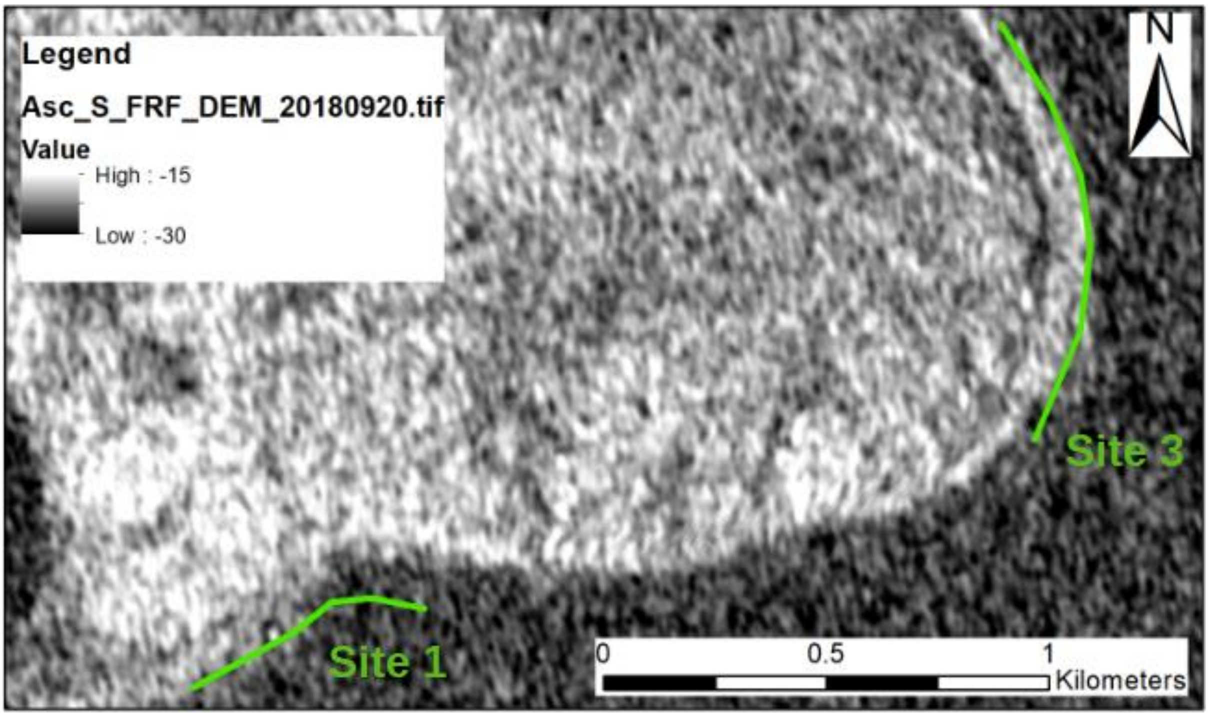

Figure 36 SAR scene based on ascending orbit from 20th September 2018 in grayscale in the background with values in dB showing the study sites 1 and 3, marked with the baselines in green. Between the baselines and the coastline there is areas of higher backscatter intensity, making accurate delineation of the coastline based only on backscatter threshold impossible. The higher noise level at the coastal areal compared to other scenes, displayed for example in Figure 21, is noticeable even at this larger map scale.

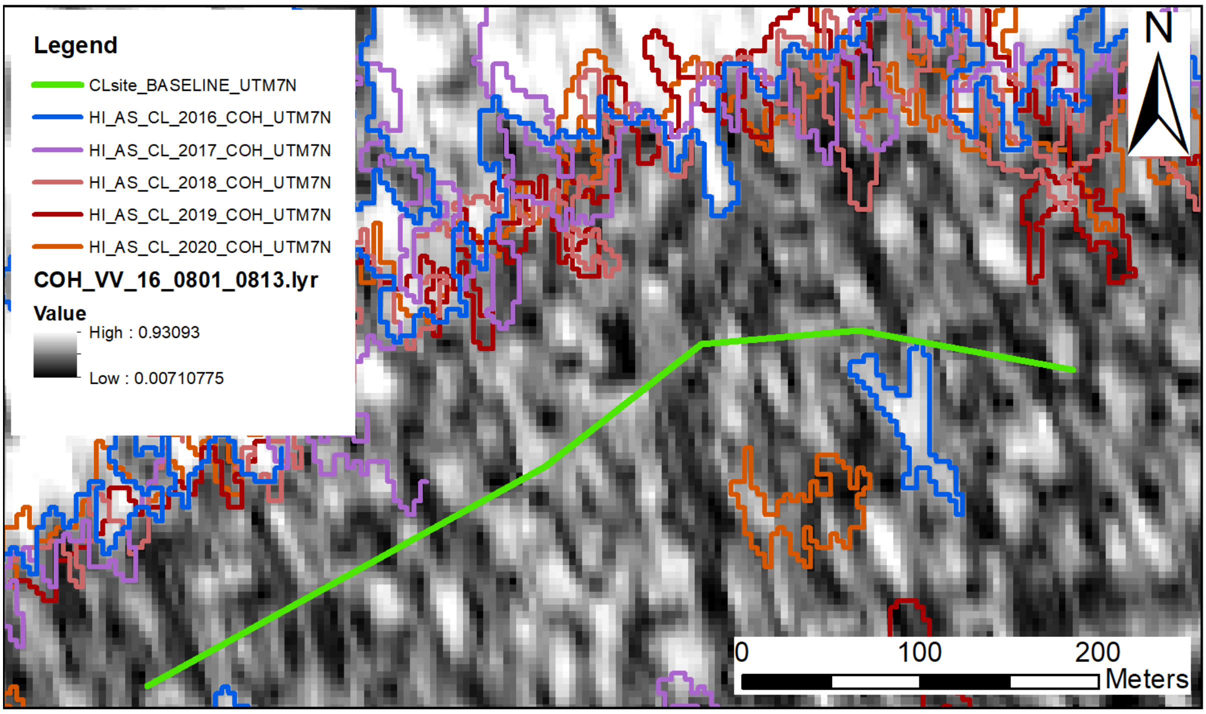

Figure 37 Estimated or sample Coherence between two SAR scenes from 2016 in greyscale. The coloured lines mark the baseline in green and the threshold boundaries from each year from blue to orange.

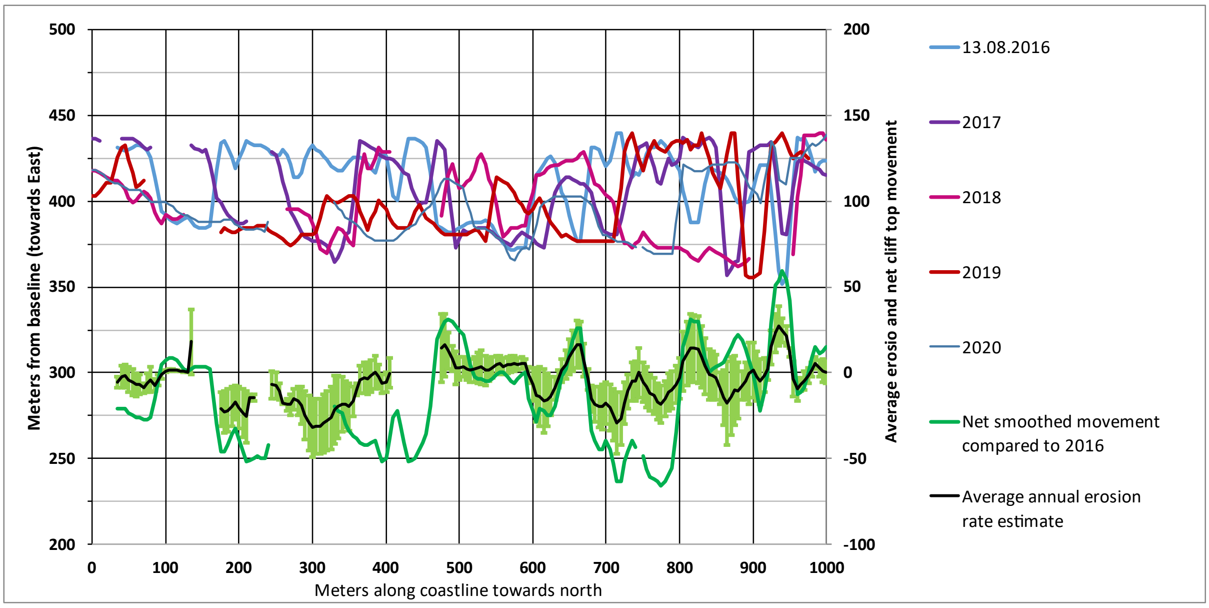

Figure 38 Coastline position estimates at Site 2. For each year from thresholding of stacked Coherence estimate from 2017 to 2020 and a single Coherence estimate from 2016 as blue to orange lines, left vertical axis. On the right axis (same scale but with an offset of 300 m) the net difference between the earliest and last position estimates (2016 and 2020) has been marked with the dark green line. Also on the right axis is the black line representing the average yearly erosion rate with the standard deviation of erosion rate estimates (green error bars) based on comparing each year with the 2016 dataset. Positive values represent erosion, negative values represent coastline progradation seawards by accumulation of sediments. The data was observed on an ascending orbit with looking direction towards East, positive y axis direction. The point spacing along the baseline is 5m, with 201 values plotted on each line.

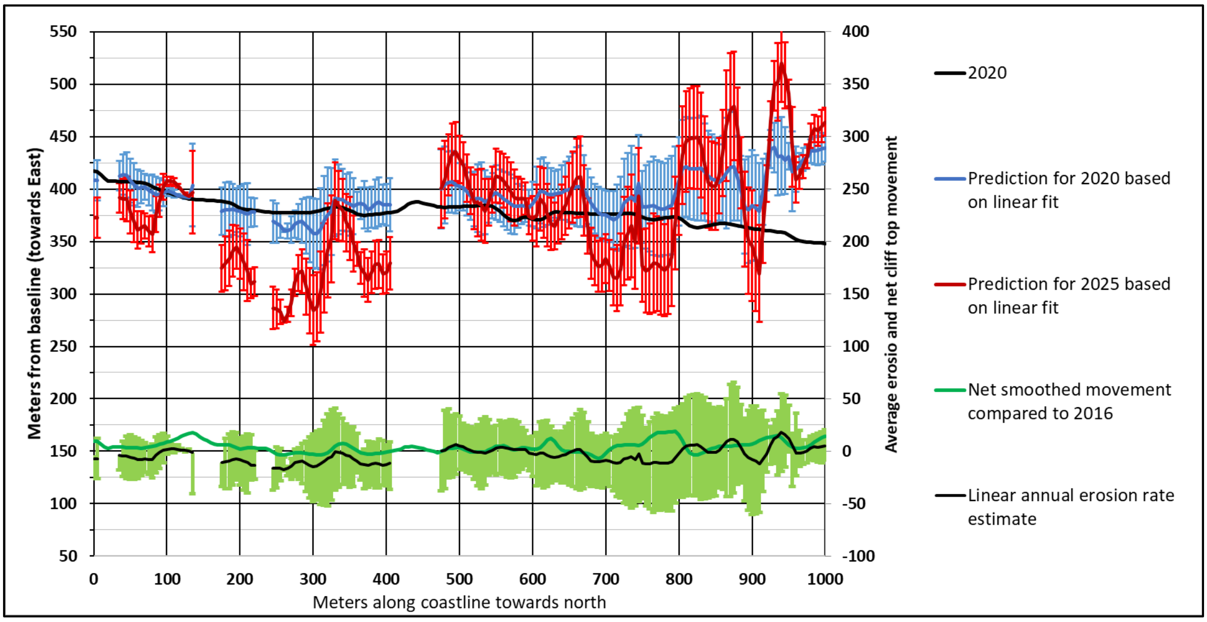

Figure 39 Coastline position estimates at Site 2. The observed 2020 position estimate (upper black line, left axis) is displayed with the estimated 2020 position from a linear fit at each point along the baseline. This estimate is based on the data displayed in Figure 38. On the right axis (same scale but with an offset of 300 m) the net difference between the earliest and last position estimates (2016 and 2020) has been marked with the dark green line. Also on the right axis is the black line (around the zero position) representing the yearly erosion rate based on the linear fit with the margin of error of the yearly erosion rate (green error bars) representing the 90% confidence interval at each point along the baseline. The data was observed on an ascending orbit with looking direction towards East, positive y axis direction. The point spacing along the baseline is 5m, with 201 values plotted on each line.

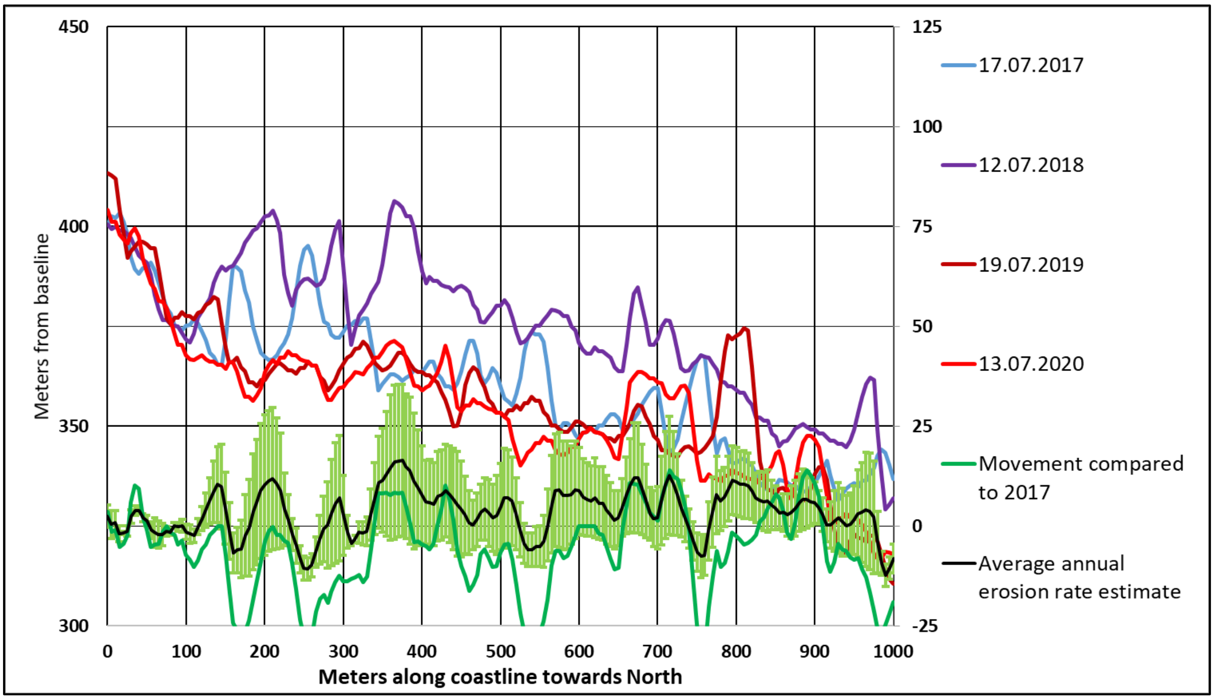

Figure 40 Site 2 – Westside: data observed on a descending orbit. The blue, purple and red lines (left vertical axis) show the coastline positions relative to the baseline, with the land side above the lines. On the right vertical axis (same scale but with an offset) is the black line representing the average erosion rates when comparing each year to the first position from 2017.Positive values represent erosion, negative values represent coastline progradation seawards by accumulation of sediments. The standard deviation of these values is given around the curve as green error bars. The darker green line (right vertical axis) shows the distance and direction of change in position between the first observed position from 2017 and the last observed position from 2020 along the Site 2 baseline. The point spacing along the baseline is 5m, with 201 values plotted on each line. The vertical axis positive direction is East.

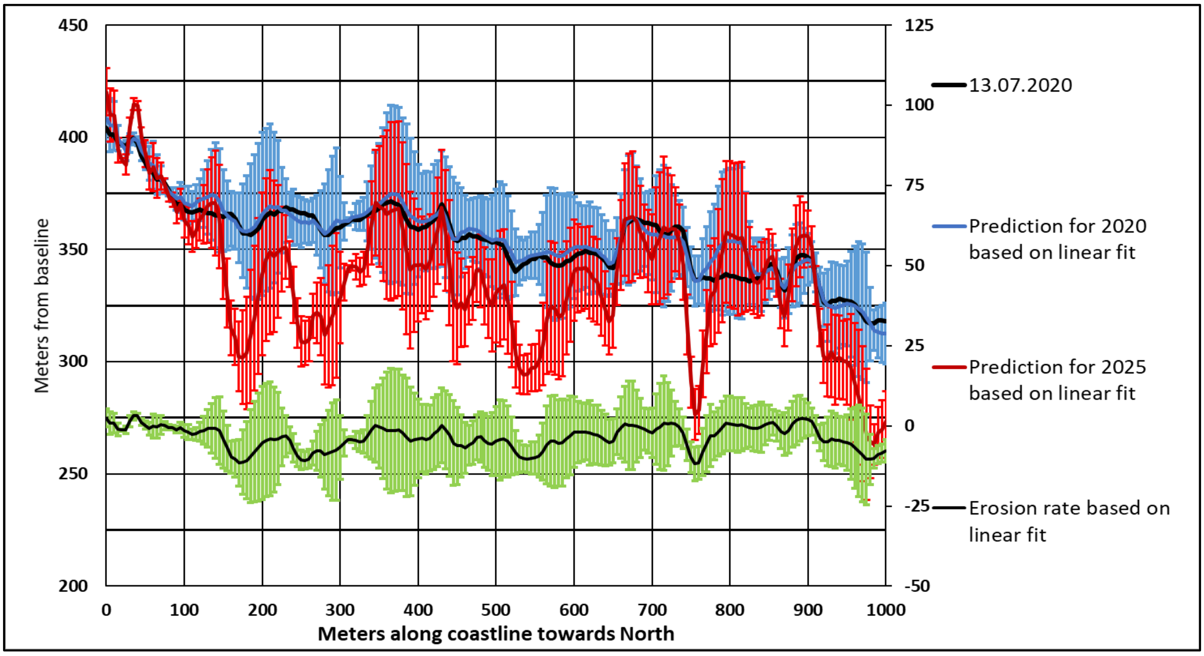

Figure 41 Site 2 – Westside: prediction of coastline positions based on data observed a descending orbit. The thicker black curve at the middle or top shows the observed coastline position for 13 July 2020 (left vertical axis) with the predicted position assuming a linear erosion rate as a blue line. The blue error bars show the two-sided 90% confidence interval around the blue line which was calculated the t-test margin of error. The predicted July 2025 coastline position is shown with the red line (left vertical axis) with the same margin of error. On the right vertical axis (same scale but with an offset) is the rate of change based on a linear fit of the data displayed as the black line at the bottom of the figure. The standard deviation of average rate of change compared to the first value from 2016 is marked around this line as green error bars. The point spacing along the baseline is 5m, with 201 values plotted on each line. The vertical axis positive direction is East.

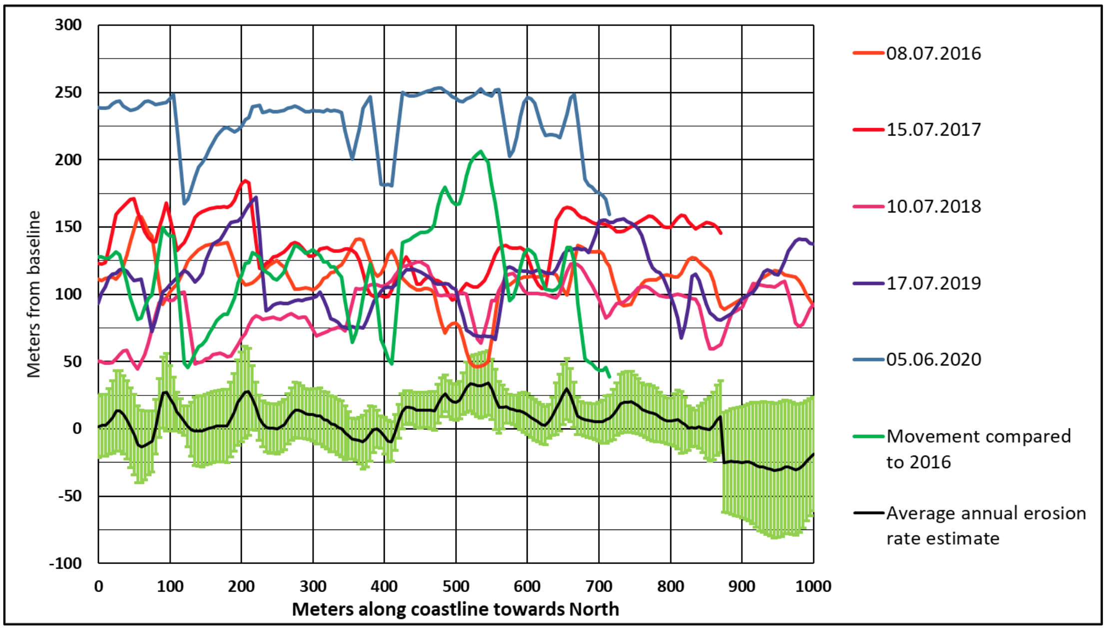

Figure 42 Site 3 – Eastside: data observed on an ascending orbit. The blue, purple and red lines show the coastline positions relative to the baseline, with the land side above the lines. The black line represents the average erosion rates when comparing each year to the first position from 2016. Positive values represent erosion, negative values represent coastline progradation seawards by accumulation of sediments. The standard deviation of these values is given around the curve as green error bars. The darker green line shows the distance and direction of change in position between the first observed position from 2016 and the last observed position from 2020 along the Site 3 baseline. The point spacing along the baseline is 5m, with 201 values plotted on each line. The vertical axis, with 25m grid lines, has been adjusted to show also outliers (blue line) and large uncertainty (green error bars) in the results. The vertical axis positive direction is North-West (left side of plot) to South-West (right side of plot) due to curved baseline.

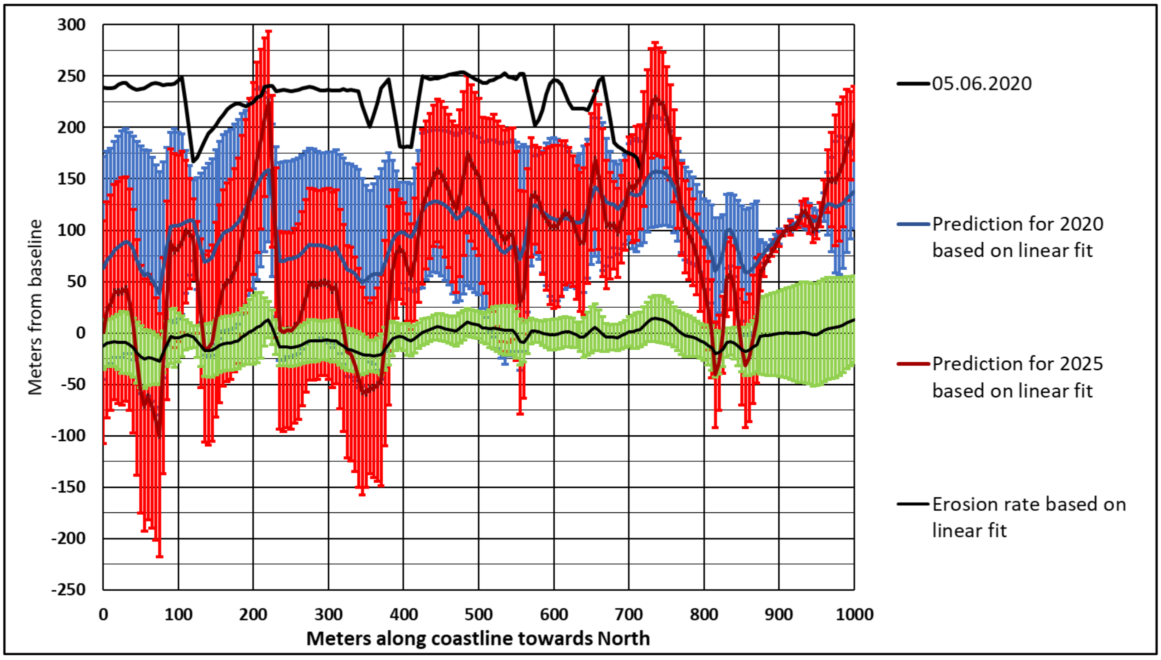

Figure 43 Site 3 – Eastside: prediction of coastline positions based on data observed on ascending orbit; landward side above lines. The black curve at the middle or top shows the observed coastline position for 05 June 2020 with the predicted position assuming a linear erosion rate as a blue line. The blue error bars show the two-sided 90% confidence interval around the blue line which was calculated the t-test margin of error. The predicted June 2025 coastline position is shown with the red line with the same margin of error. The rate of change based on a linear fit of the data displayed as the black line at the bottom of the figure. The standard deviation of average rate of change compared to the first value from 2016 is marked around this line as green error bars. The point spacing along the baseline is 5m, with 201 values plotted on each line. The vertical axis range has been further expanded to show the large margin of error around the 2025 position prediction. The vertical axis positive direction is North-West (left side of plot) to South-West (right side of plot) due to curved baseline.

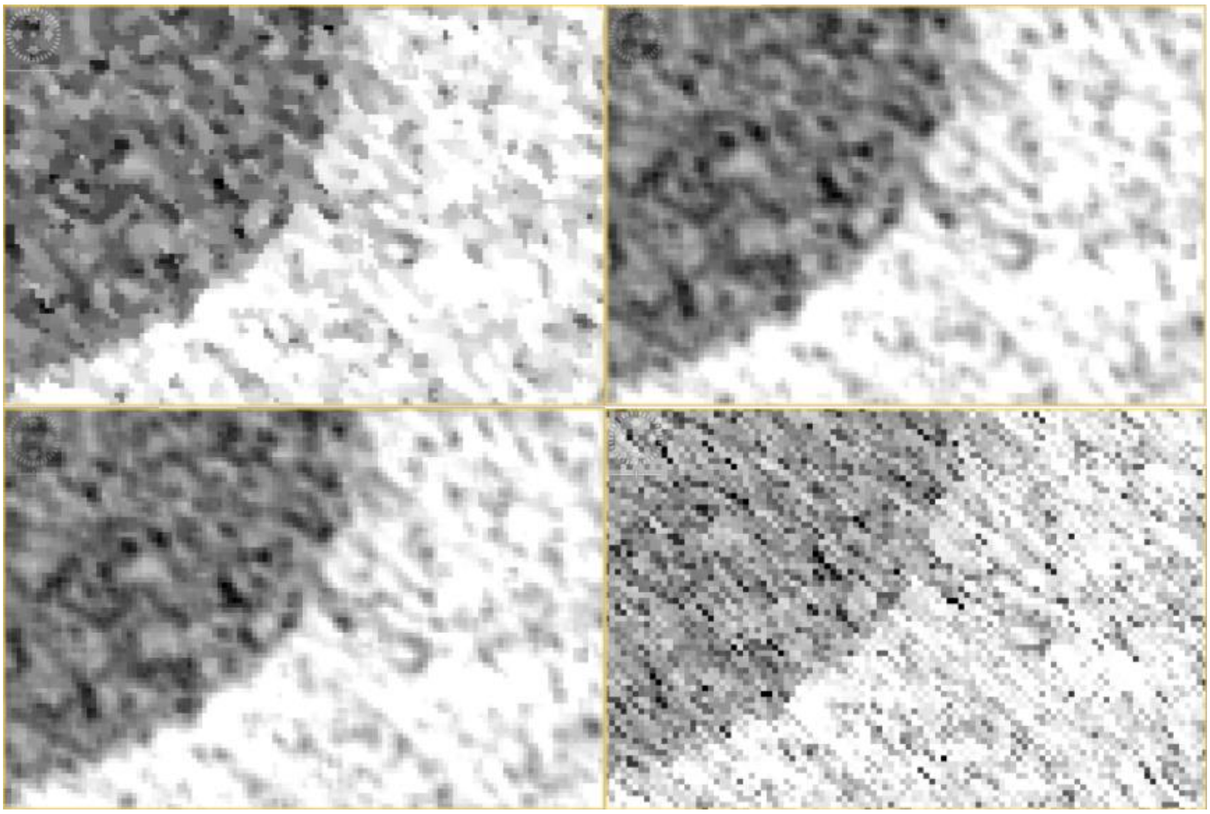

Figure 44 Comparison of three filters applied to the SAR scene at sight 1 with backscatter intensity. Top-left: Median filter result showing very clear contours but also more noise-related structures. Top right: Gamma filter result showing more smoothing but still preserving structures, with more noise suppression. Bottom left: Frost filter result, showing very similar properties to top right. Bottom right: The unfiltered SAR scene, showing noise at the individual pixel level.

Table 4 General information for the datasets used for Backscatter thresholding: Orbital path or looking direction, date of acquisition and thresholds used for Site 1 and Site 2 and 3, with lastly remarks about the noise level and general SAR image quality. Only Backscatter with VV polarisation was used, as the VH polarisation was not available for all datasets, differences between the data from both polarisations are generally quite small however, the images having close to the same characteristics.

Ascending (A) or Descending (D) orbit	**Date of acquisition**	**Threshold value in dB specifically for study site 1: CL site**	**Threshold value in dB for entire Island used at Site 2 and 3**	**Data quality remarks**
Summer season: June-September				
A	20.9.2018	-19.5	/	data unusable
A	8.7.2016	-22.5	-22	
A	15.7.2017	-22.5	-22.5	
A	10.7.2018	-22.5	-22.5	
A	17.7.2019	-23	-23	
A	5.6.2020	-21	-21	
D	17.7.2017	-24	-24	
D	12.7.2018	-23.5	-23.5	
D	19.7.2019	-22.5	-25.5	
D	13.7.2020	-25	-25	-
Winter season: December-April				
A	16.3.2015	-24	/	data unusable
A	15.4.2016	-24.75	/	low quality, high result variance
A	5.3.2017	/	/	data unusable
A	10.4.2017	-24.7	/	low quality, high result variance
A	17.4.2018	-24.75	/	
A	31.3.2019	-25.9	/	low quality
A	25.3.2020	-26	/	low quality
A	12.2.2021	-24	/	low quality/ high result variance
D	24.12.2014	-22	/	data unusable
D	31.12.2016	-18	/	data close to unusable
D	20.12.2017	-18	/	low quality
D	27.12.2018	-26.2	/	low quality
D	22.12.2019	-27	/	
D	28.12.2020	-27.5	/	low quality

Table 5 General information about datasets and thresholds used for monitoring coastline positions based on normalised Coherence, with range [0, 1].

Year of stacked coherence estimate	**Date of acquisition for SAR scenes on which the Coherence estimate is based**	**Threshold value for Site 1**	**Threshold value for Site 2**
2016	01.08.2016	0.46	0.46
	13.08.2016		
2017	07.10.2017	0.46	0.45
	22.07.2017		
	08.08.2017		
	25.09.2017		
2018	10.07.2018	0.46	0.45
	22.07.2018		
	03.08.2018		
	15.08.2018		
	27.08.2018		
2019	05.07.2019	0.46	0.46
	17.07.2019		
	29.07.2019		
	10.08.2019		
	22.08.2019		
2020	11.07.2020	0.46	0.46
	23.07.2020		
	04.08.2020		
	16.08.2020		
	28.08.2020		
	09.09.2020		
	21.09.2020		
Path	**79**		
Frame	**226**		